A Bottom-Up, Multi-Scale Theory for Transient Mass Transport of Redox-Active Species through Porous Electrodes beyond the Pseudo-Steady Limit

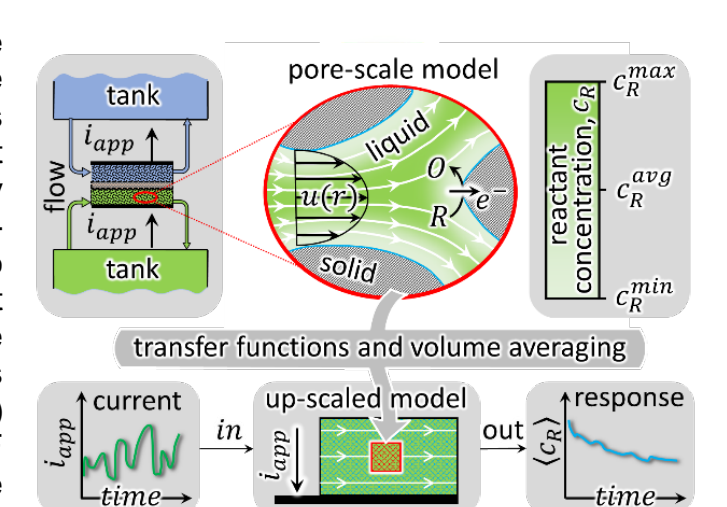
Md Abdul Hamid^a and Kyle C. Smith^{a,b,c,d,*}

- ^a Department of Mechanical Science and Engineering, University of Illinois at Urbana-Champaign, Urbana, IL 61801, USA
- ^b Department of Materials Science and Engineering, University of Illinois at Urbana-Champaign, Urbana, IL 61801, USA
- ^c Computational Science and Engineering Program, University of Illinois at Urbana-Champaign, Urbana, IL 61801, USA
- ^d Beckman Institute for Advanced Science and Technology, University of Illinois at Urbana-Champaign, Urbana, IL 61801, USA

*Corresponding author: kcsmith@illinois.edu

Abstract

New theory is presented for the dynamic response of redox-active electrolyte flowing through porous electrodes under time-dependent applied current. This is done by introducing certain frequencydependent transfer functions (TFs) to pore-scale up-scale transport phenomena. One TF – dubbed the spectral Sherwood number – extends the film law of mass transfer (FLoMT) to transient conditions. Another TF captures the acceleration/suppression of solute



advection that results from pore-scale velocity/concentration gradients. Numerical results are shown for the frequency-dependent TFs of solid cylinders in crossflow to represent porous electrodes commonly used in FBs. Spectral regions are observed where a transition from lagless response to semi-infinite Warburg response occurs with increasing frequency. The embedding of these TFs into an up-scaled model is also formulated to obtain the time-domain response of FBs. Without adjustable parameters this model predicts polarization in agreement with transient flow-battery (FB) experiments, despite systematic overprediction of polarization by the conventional FLoMT model. Analysis of concentration polarization and reactant concentration is also used to construct non-dimensional maps of operational space. These predictions show that fast current fluctuations are sustained even when current exceeds the limiting current expected from the time-invariant FLoMT without solute advection suppression/acceleration, suggesting implications for electrochemical conversion and separations devices in addition.

Keywords: flow battery, concentration polarization, transfer function, over-limiting current

1. Introduction

Renewable energy sources are projected to comprise approximately 60% of US electricity generation by 2050, with wind and solar power contributing approximately 2000 and 1000 TW-h respectively [1]. Electricity generation from wind and solar power plants requires installation of large-scale energy-storage devices to overcome the mismatch between electricity demand and intermittent supply arising from the stochastic nature of wind and the diurnal cycle of solar insolation [2]. Redox flow batteries (RFBs) have drawn attention due to their ability to independently scale power and energy-storage capacity because of the modularity of their reactors that dictate power capability and of their tanks that dictate energy-storage capacity. Here, redox-active liquid electrolyte is circulated through RFB electrodes to and from tanks, forming a closed loop. Despite advances in RFB electrolyte chemistry [3–7], the surface chemistry of their electrodes [8–15], and the design of flow fields [16-20], limited understanding has been established to date concerning the impact of the inherently transient and irregular charge/discharge scenarios that RFBs are likely to experience on renewable-powered grids and micro-grids. For instance, past RFB models have adopted a film law of mass transfer using a timeindependent mass transfer coefficient to predict pore-scale concentration polarization and associated energy losses (e.g., in Refs. [16,21-25]).

Here, we posit that understanding of such concentration polarization must start from the bottom-up at the scale of the electrode pores at the surfaces on which redox reactions take place, in concert with the flow of electrolyte and the transport of soluble species occurring therein. Because all three modes of soluble species transport (diffusion, advection, and migration) contribute to total flux, the time variation of current and cell voltage – induced by the instantaneous power supplied to or demanded from the cell incorporating that electrode - drives the associated transport of species in solution via redox reactions at electrode surfaces. Here, the power spectral density (PSD) distribution associated with any given power-supply or -demand entity indirectly captures their transient and stochastic qualities using a frequency-based representation [26,27]. Wind power experiences an especially wide PSD distribution relative to other renewable sources [26], stemming from the occurrence of gusts (~1 Hz [26]) and daily weather (~0.1 to 1 mHz). For the sake of comparison, a typical aqueous all-vanadium RFB (diffusivity $D\sim10^{-6}$ to $10^{-7}cm^2/s$ [28–31]) with carbon-felt electrode (fiber diameter $b\sim10$ to $20~\mu m$ [32,33]), has a characteristic frequency $f_c = D/b^2 \sim 0.025$ to $1\,Hz$. Further, the low diffusivity of active species in non-aqueous electrolytes (e.g. $D=10^{-10}\ cm^2/s$ in deep eutectic solvent [34]) can decrease f_c by orders of magnitude. Overlap between the ranges of f_c with the PSD distribution of wind, therefore, suggests that the frequencydependent response of RFBs is likely to play an important role in the efficient utilization of wind energy.

Despite its potential importance for grid-scale energy storage with RFBs, limited theoretical understanding of solution-phase frequency response has been established at the pore-scale in modeling and experimentation. Beyond the film-law of convection mass transfer, time-domain pore-scale simulations have been conducted using the lattice Boltzmann method [35,36], but rigorous up-scaling strategies have yet to be developed to enable the simulation of transient transport phenomena at scales larger than

representative volume elements. In contrast, a recent approach used Laplace transformation to analyze the transient redox and diffusion of vanadium-based activespecies in stagnant electrolytes at carbon-felt electrodes during cyclic voltammetry [37]. We also recently introduced theory [38] to capture the effect of charge/discharge at the pore-scale for active species undergoing simultaneous diffusion and advection in the pseudo-steady limit, which is approached when the characteristic time period for a charge/discharge cycle $au_{c/d}$ is large relative to the characteristic diffusion time-scale (i.e., $\tau_{c/d} \gg b^2/D$). Previous work on stationary batteries has used a frequency-based formalism to predict transient dynamics of solid-state diffusion processes [39] and to model electrochemical impedance spectra [40-42]. In this article we introduce a new theory for modeling transient pore-scale mass transfer with simultaneous convection and redox reactions using a frequency-response formalism for the first time that enables direct up-scaling of the coupling between pore-scale concentration polarization and temporal variations of current supply and demand. In this article, we do this by defining a new spectral Sherwood number transfer function $\langle \widetilde{Sh} \rangle$ that relates average surface flux $\langle j \rangle_s$ (i.e., reaction rate) to the associated concentration difference at the pore-scale $\Delta c = c_s$ $\langle c \rangle$ in the frequency domain: $\langle \widetilde{Sh} \rangle \equiv \langle \overline{j} \rangle_s (b/D)/(\overline{c}_s - \langle \overline{c} \rangle)$, where \overline{A} is the continuous-time Fourier transform of quantity A, b is a characteristic pore length-scale, and D is diffusivity.

The rate capability of electrochemical devices is determined by the amount of electric current produced and various mechanisms of polarization. In RFBs and other devices using flow-through electrodes (e.g., electrochemical deionization [43-45]), continuous supply of fresh electrolyte to electrode pores and the simultaneous evacuation of spent electrolyte from electrode pores is facilitated by bulk flow, i.e., advective flux. The advective flux of soluble species is affected by their depletion or accumulation near reacting interfaces where such species are respectively consumed or produced. Previous models of electrochemical devices using flow-through electrodes have adopted a macrohomogeneous advection-reaction-dispersion(-migration) (ARD(M)) theory, building on earlier geochemical theory and practice [46], that implicitly assumes that the local volumeaveraged solute concentration is advected by the bulk superficial velocity of electrolyte [24,25,43-45]. In contrast, previous modeling of unconventional RFBs using mixedconducting suspensions flowing through open channels - rather than flowing liquid electrolyte through porous electrodes – showed that coulombic and energy efficiency can be enhanced by uniformizing advective transport via the control of interfacial slip [47]. rheology [47-49], and fluid pulsation [47,48,50], the effects of which are not captured by conventional ARD(M) theory. Studies motivated by other applications have previously modeled the effects of interfacial reactions on advection in porous media by accounting for the difference between mean solute velocity and mean solvent velocity caused by the inhomogeneity in solute concentration across pores [51,52]. The prediction of such was accomplished in the long-time limit using the method of moments [53-55], where an adjoint eigenvalue problem coupled to a closure problem was solved numerically to obtain the mean solute velocity, reactivity coefficient, and dispersion tensor in a self-consistent manner [55]. In contrast, the approach that we use in this article is to characterize the integral covariance between the pore-scale velocity field and the pore-scale concentration field obtained from solutions to the Fourier-transformed mass conservation equations (MCEs), inspired by rigorous theory of pore-scale averaging [56]. We ultimately express

this covariance using a non-dimensional average advective-flux transfer function $\langle N \rangle \equiv (1/|u_s|)(u_s\langle \bar{c} \rangle - \varepsilon \langle u\bar{c} \rangle)/(\bar{c}_s - \langle \bar{c} \rangle)$ that quantifies the deviation of average advective flux $\varepsilon \langle uc \rangle$ from the product of average concentration and superficial velocity $u_s\langle c \rangle$.

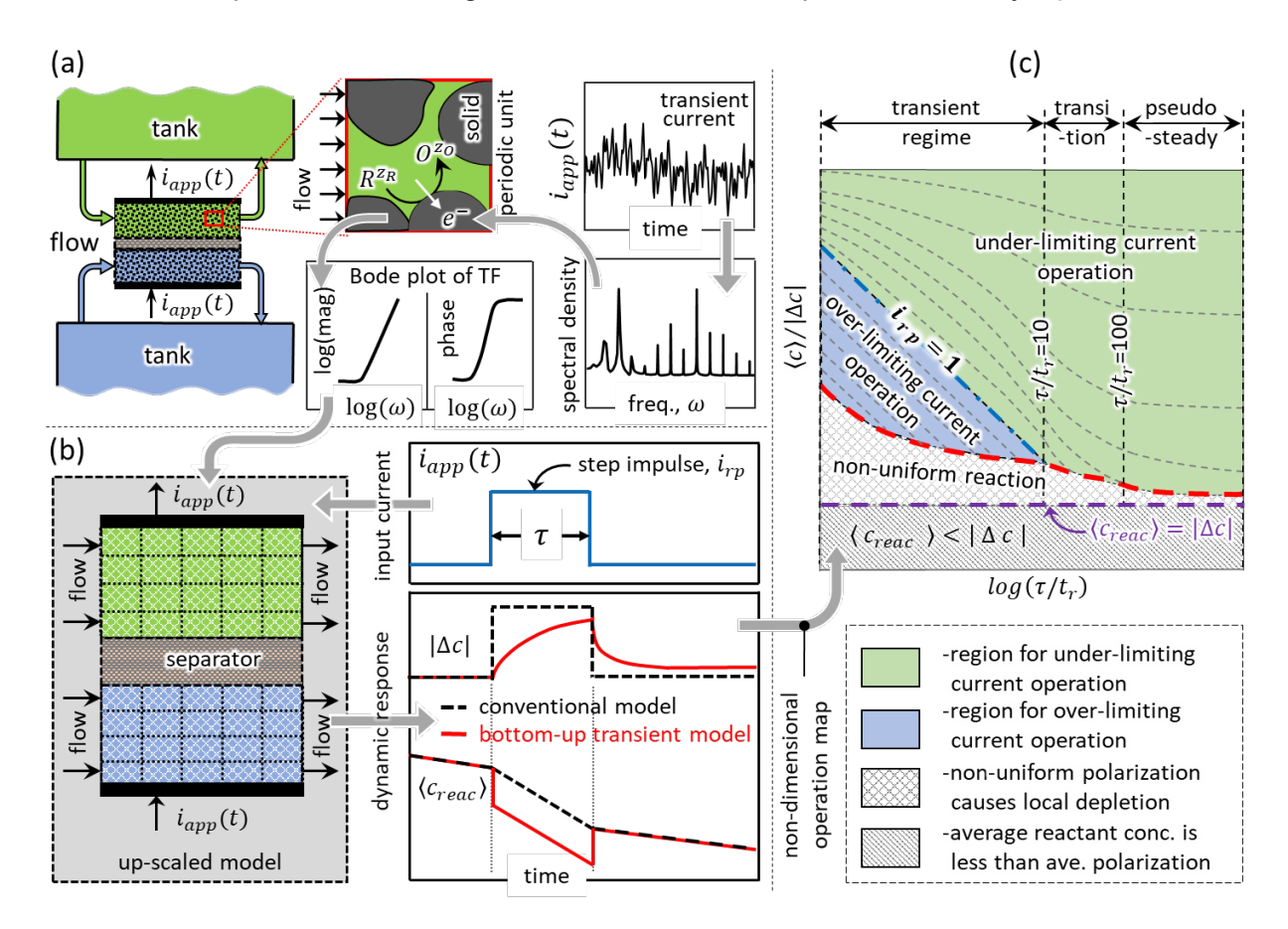


Fig. 1. (a) Illustration of a redox flow battery with flow-through porous electrodes containing electrolyte with close-up view at the micro-scale pores where redox-active species R and O are dissolved. Transient current with arbitrary time-dependence is mapped to the frequency domain using Fourier transformation to obtain a spectral density for current, and frequency-dependent transfer functions (TFs) are used to capture the microscopic response of the RFB in the frequency domain, which are later embedded into a macroscopic model. (b) Macroscopic model formulation using porous electrode theory, where the dynamic response is captured through variation of polarization magnitude $|\Delta c|$ and average reactant concentration $\langle c_{reac} \rangle$ with time for a step impulse input current. (c) Schematic of transient RFB operation based on the dynamic response of $|\Delta c|$ and $\langle c \rangle$ inside a porous RFB electrode.

In this article we present new theory for the transient response of redox-active electrolyte in porous electrodes using frequency-dependent transfer functions (TFs) that we show are readily up-scalable. These TFs link the Fourier transform of output parameters (reaction rates and advective flux deviation) to that of input parameters (surface concentration and volume-averaged concentration). We use these TFs to capture the microscopic response of RFB electrodes in the frequency domain under

varying current input at the reactive interface. Later these frequency-dependent TFs are embedded into an up-scaled model (using porous electrode theory) to obtain the macroscopic response of RFBs. A schematic representation of the approach is shown in Fig. 1. In Sec. 2 the definitions of these TFs are derived by Fourier transformation of the corresponding mass conservation equations (MCEs), which are first defined in the time domain. Then the macro-scale MCEs based on porous electrode theory are presented, where pore-scale responses are incorporated using the TFs derived earlier. In Sec. 3 the developed transient model is compared with the experiments using transient operation of a ferro/ferri-cyanide based flow cell with microchannels engraved in graphite foil. Finally, the obtained pore-scale and macro-scale MCEs are solved numerically for different porosity (ε) and Péclet number (Pe) values using electrodes comprised of cylinders in crossflow. The results obtained from pore-scale simulations are presented in Sec. 4. In Sec. 5 numerically obtained macroscopic responses of RFBs under step impulse variation of input current are presented for two different porosity electrodes. For interested readers derivations for the conditions of validity of this theory, a proof of the equivalence between the limit of vanishing frequency and the pseudo-steady limit, numerical model implementation, and model verification are presented in the supplementary information.

2. Methods

Here we present theory for the modeling of pore-scale transfer functions in the frequency domain and for their incorporation into a macro-scale model of RFB electrodes in the time domain. We do this by defining the pore-scale problem in the time domain and by subsequently converting it to the frequency domain using the Fourier transform to yield spectral Sherwood number and advective flux transfer functions. The macro-scale model incorporates concentration polarization and advective flux within electrode pores using state-space approximations of the aforementioned pore-scale transfer functions under time-varying applied current. Derivations used to obtain the above models and the numerical methods used to solve the governing equations at both scales are in the supplementary information.

2.1. Governing equations for pore-scale transport

In this section we present the governing equations for electrolyte containing a soluble redox couple undergoing redox at electrode surfaces. The mass conservation equations (MCEs) and associated boundary conditions (BCs) governing the evolution of the pore-scale concentration field within electrode pores are presented in the time domain and are transformed into the frequency domain to derive transfer functions (TFs) for reactive advective flux. We note that similar and analogous equations govern the transport of other electrochemical, chemical, and thermal systems, but we focus here on the specific application of the present theory to RFBs.

2.1.1. Time-domain governing equations

For electrochemical systems that use heterogenous electron transfer reactions involving a soluble redox couple $(R^{z_R} \rightleftharpoons O^{z_O} + e^-)$, as in RFBs, the consumption of reduced species R is coupled with the production of oxidized species O. We neglect the

electromigration contributions to the net flux provided that the transference number of any participating soluble species is sufficiently small [38]. Under such condition we show subsequently that the theory that we presented previously [38] can be extended to incorporate arbitrary time-variation of the surface concentration $c_{i,s}(t)$ of species i when the associated Damköhler numbers $(Da_{red/ox} = k_{red/ox} \, b/D)$ for reduction and oxidation reactions are sufficiently large: $Da_{red} \gg \min[1, exp(-F\eta/RT)]$ and $Da_{ox} \gg \min[1, exp(F\eta/RT)]$, where η is a characteristic overpotential and RT/F is the thermal voltage. The derivation of these criteria using scaling analysis is presented in the supplementary information. Under such conditions the conservation of mass for species i is written as:

$$\frac{\partial c_i}{\partial t} + \nabla \cdot (\boldsymbol{u}^{\bullet} c_i - D_i \nabla c_i) = 0; \qquad c_i|_{s} = c_{i,s}(t)$$
 (1a)

Here, c_i is the concentration of soluble redox-active species i, which depends on position r and time t, D_i is its corresponding Fickian diffusion coefficient, and u^{\blacksquare} is the molar-volume averaged fluid-velocity vector. Further, we assume that the characteristic streamwise concentration difference is negligible relative to the characteristic pore-scale concentration difference through the microstructure of porous electrode, as in our previous work [38]. Such an assumption enables us to use periodic BCs at the boundaries of the repeat units of periodic microstructures:

$$c_i(\mathbf{r},t) = c_i(\mathbf{r} + \mathbf{R},t), \tag{1b}$$

where R is any integer-multiple linear combination of lattice vectors defining the microstructure's periodicity. By analyzing the time-dependent dynamics of RFBs cycled under galvanostatic conditions we showed previously that the validity of such a condition depends on the respective magnitudes of the Sherwood number $\langle Sh \rangle$, Péclet number Pe, and Fourier number $Fo = Dt/b^2$ [38]. For the limit of vanishing Fo this condition requires $\langle Sh \rangle \ll (L_r/b)/Fo$, which allows the use of the periodic BC expressed in Eq. 1b for high Pe flows where the associated characteristic frequency of the transient current is large. Under such conditions solute transport is controlled by a fast-changing surface concentration, and the effect of streamwise concentration differences is negligible in the entrance region where the local concentration field develops. In this section, we invoke periodic boundary conditions in an $ad\ hoc$ manner motivated by the arbitrariness of the surface condition imposed. However, after defining the spectral Sherwood number and the nondimensional advective flux transfer function, we derive a new criterion for this assumption to be valid using scaling analysis in the frequency domain (see supplementary information).

¹ Throughout this article i as a subscript indicates either species R or O, while i otherwise indicates current density.

² We model the bulk electrolyte as *isochoric*, such that the pore-scale molar-volume averaged fluid-velocity u^{\blacksquare} is divergence free (i.e., $\nabla \cdot u^{\blacksquare} = 0$) [38].

2.1.2. Frequency-domain governing equations and pore-scale transfer functions

Using the time-domain governing equations from Sec. 2.1.1, we show that certain transfer functions (TFs) can be used to succinctly capture the transient response of output parameters to both the surface- and volume-averaged solute concentrations. To do so, the MCEs that govern concentration fields are reduced to a set of linear partial differential equations (PDEs) in the frequency domain using the continuous-time Fourier transform. Using this approach, we define TFs for the average surface flux and the average advective flux, the former of which we show is a kind of *spectral* Sherwood number $\langle \widetilde{Sh} \rangle$ that depends on frequency and the latter of which $\langle N \rangle$ captures the integral covariance between pore-scale velocity and the Fourier-transformed concentration fields.

2.1.2.1. Fourier transformed governing equations

Fourier transformation of the MCEs and the BCs expressed in Eq. 1 results in a steady, linear PDE that governs the Fourier transformed species concentration \bar{c} while the solid/solution interface is subjected to a time-varying sinusoidal surface concentration with angular frequency $\omega = 2\pi f$ in rad/s, where f is regular frequency in Hz. In general, Fourier transformed functions are denoted here by an overbar (i.e., $\mathcal{F}\{A(t)\} = \bar{A}(\omega) = \int_{-\infty}^{+\infty} A(t) exp(-j\omega t) dt$, where A(t) is an arbitrary function of time). The Fourier transformed version of Eq. 1 is given by:

$$\nabla \cdot (\boldsymbol{u}^{\bullet} \bar{c}_i - D_i \nabla \bar{c}_i) + j \omega \bar{c}_i = 0; \qquad \bar{c}_i|_{s} = \bar{c}_{i,s}(\omega), \qquad (2)$$

where $j=\sqrt{-1}$ is the imaginary unit. Frequency response of the corresponding system's concentration field is captured by a transfer function $\mathbb{C}_i(\omega, \mathbf{r})$ defined with $\bar{c}_i(\omega, \mathbf{r})$ as its output quantity and with $\bar{c}_{i,s}(\omega)$ as its input quantity:

$$\mathbb{C}_{i}(\omega, \mathbf{r}) \equiv \frac{\bar{c}_{i}(\omega, \mathbf{r})}{\bar{c}_{i,s}(\omega)} \tag{3}$$

Substituting $\bar{c}_i(\omega, \mathbf{r}) = \bar{c}_{i,s}(\omega)\mathbb{C}_i(\omega, \mathbf{r})$ into Eq. 2 results in a time-independent PDE for \mathbb{C}_i with a frequency-independent interfacial condition:

$$\nabla \cdot (\boldsymbol{u}^{\bullet} \mathbb{C}_{i} - D_{i} \nabla \mathbb{C}_{i}) + j \omega \mathbb{C}_{i} = 0; \qquad \mathbb{C}_{i}|_{s} = 1. \tag{4}$$

For $D_O = D_R$ inspection reveals that the dynamic responses of R and O are identical ($\mathbb{C}_R = \mathbb{C}_O$). To establish a necessary condition to ensure the coupled production and consumption of R and O we invoke reaction stoichiometry:

$$D_R \frac{\partial \bar{c}_R}{\partial n} \Big|_{s} = -D_O \frac{\partial \bar{c}_O}{\partial n} \Big|_{s} \Rightarrow D_R \left. \bar{c}_{R,s} \frac{\partial \mathbb{C}_R}{\partial n} \right|_{s} = -D_O \left. \bar{c}_{O,s} \frac{\partial \mathbb{C}_O}{\partial n} \right|_{s}$$
 (5)

From this expression we deduce that $\bar{c}_{R,s} = -\bar{c}_{0,s} = \bar{c}_{i,s}$ enforces the conjugation condition exactly when $D_R = D_0$ is satisfied. We note that changing the sign of $\bar{c}_{i,s}$ does not change the associated PDEs and BCs (Eq. 4) that govern $\mathbb{C}_i(\omega, r)$. Thus, identical PDEs for O

and R automatically enforce the coupled production/consumption of active species when posed in terms of \mathbb{C}_i (Eq. 4).

We now elaborate on the physical significance of the transfer function $\mathbb{C}_i(\omega,r)$. Since the interface condition that is controlled by $\bar{c}_{i,s}$ corresponds to a sinusoidal, periodic disturbance signal in the time domain, Eq. 4 governs the propagation of this disturbance throughout the electrolyte solution. The transient response at a location r is captured by the magnitude and phase of \mathbb{C}_i that respectively represent the fractional concentration change and phase lag with respect to the change made in surface concentration $c_{i,s}$. For example, at an interface the conditions $|\mathbb{C}_i|=1$ and $\theta_{\mathbb{C}_i}=0$ imply that the concentration there tracks the imposed $c_s(t)$ boundary condition instantly. On the contrary $\mathbb{C}_i=0$ at some arbitrary location suggests that the interfacial disturbance induced by time-varying $c_{i,s}$ is not experienced there. Hereafter, we drop the subscript i from the various parameters of interest because the various species of interest exhibit identical governing equations for \mathbb{C}_i .

2.1.2.2. Spectral Sherwood number

The steady response of solution undergoing convective mass transfer with simultaneous reactions in porous media has historically been captured using an overall Sherwood number $\langle Sh \rangle = \langle h_m \rangle b/D$, with $\langle h_m \rangle$ being the overall mass transfer coefficient that relates the average surface flux $\langle j \rangle_s = D \langle \partial c/\partial n|_s \rangle$ due to reactions to a driving concentration difference Δc , according to the film law of mass transfer: $\langle j \rangle_s = \langle h_m \rangle \Delta c.^3$ The operators $\langle ... \rangle$ and $\langle ... \rangle_s$ are respectively integral averages over solution volume and solid/solution interfaces contained in a representative volume element. To our knowledge, however, similar theory has yet to be developed that captures the *transient* response of solutions undergoing convective mass transfer in porous media. It is our goal presently to predict average reaction rates vis-à-vis average surface flux subjected to an arbitrary time-varying surface concentration to enable up-scaling in volume-averaged/macrohomogeneous formulations (cf. Ref. [56]) in a manner that is consistent with transient pore-scale transport phenomena.

To do this we derive a transfer function in the frequency domain that extends the concept of the Sherwood number to transient conditions. This particular Sherwood number, which we call a *spectral Sherwood number* (\widetilde{Sh}) , is a transfer function in the

_

³ Established theory and experiment [74–76] have previously shown that $\langle Sh \rangle$ principally depends on Péclet number $Pe = |\mathbf{u}_s|b/D$, where \mathbf{u}_s is superficial velocity, and on the Schmidt number Sc = v/D, where v is kinematic viscosity. In porous materials undergoing forced convective heat transfer, the Nusselt number $\langle Nu \rangle = \langle h \rangle b/k$, with overall heat transfer coefficient $\langle h \rangle$ and thermal conductivity k, is equivalent to $\langle Sh \rangle$ by virtue of the formal analogy between the equations governing heat and mass transfer when the Prandtl number $Pr = v/\alpha$ with thermal diffusivity α and the thermal Péclet number $Pe_t = |\mathbf{u}_s|d/\alpha$ are respectively used in place of Sc and Pe.

frequency domain that captures the correlation between average surface flux $\langle \bar{\jmath} \rangle_s$ and the characteristic concentration difference $\Delta \bar{c} = \bar{c}_s - \langle \bar{c} \rangle$:

$$\langle \widetilde{Sh} \rangle (\omega) \equiv \frac{b}{D} \frac{\langle \overline{\jmath} \rangle_S}{\overline{c}_S - \langle \overline{c} \rangle} = \frac{-\langle \partial \mathbb{C} / \partial n^* \rangle}{1 - \langle \mathbb{C} \rangle} = \frac{\langle G \rangle}{1 - \langle \mathbb{C} \rangle}$$
(6)

Here, the nondimensional normal coordinate is $n^* = n/b$, and $G(\omega,r)$ is a gradient transfer function defined as $G(\omega,r) \equiv (b/D)(\bar{\jmath}_s/\bar{c}_s) = -\langle \partial \mathbb{C}/\partial n^* \rangle$ with input as surface concentration \bar{c}_s , rather than $\Delta \bar{c} = \bar{c}_s - \langle \bar{c} \rangle$.⁴ With $\langle \widetilde{Sh} \rangle$ known from pore-scale simulation, the average surface flux $\langle \bar{\jmath} \rangle_s$ can be determined in the time domain as $\langle \bar{\jmath} \rangle_s = (D/b)\mathcal{F}^{-1}\{\langle \widetilde{Sh} \rangle(\bar{c}_s - \langle \bar{c} \rangle)\}$, according to Eq. 6.

For the sake of consistency with the definition of the Sherwood number obtained in the pseudo-steady limit [38], we confirm presently that the spectral Sherwood number $\langle \widetilde{Sh} \rangle$ obtained in the limit of vanishing frequency is identical to the conventional $\langle Sh \rangle$ in the pseudo-steady limit: $\lim_{\omega \to 0} \langle \widetilde{Sh} \rangle = \langle Sh \rangle_{PSL}$. A detailed proof demonstrating this property of $\langle \widetilde{Sh} \rangle$ is shown in the supplementary information. This result thus provides intuition for the broader meaning of the pseudo-steady limit in the context of frequency response. As we later demonstrate using numerical modeling, the limit of vanishing frequency is equivalent to the pseudo-steady limit because concentrations and fluxes exhibit lagless tracking (i.e., vanishing phase difference) with time variations of surface concentration in that limit.

2.1.2.3. Advective-flux transfer function

We now define a transfer function that quantifies the transient response of average advective flux to the pore-scale concentration difference $\Delta c = c_s - \langle c \rangle$. Previously derived volume-averaging theory for pore-scale transport suggests that the local volume-averaged advective flux $\langle u^{\blacksquare}c \rangle$ should be decomposed into terms that account for the average contribution to velocity and concentration, as well as those that result from the deviation of those parameters from their averages [56,57]. In contrast, we characterize $\langle u^{\blacksquare}c \rangle$ presently by defining the integral covariance vector $\langle W \rangle$ for velocity u^{\blacksquare} and concentration c, thus avoiding the introduction of ad hoc assumptions that are needed to decompose $\langle u^{\blacksquare}c \rangle$ into an arbitrary sum of products between average and deviatoric u^{\blacksquare} and c fields:

$$\langle \boldsymbol{W} \rangle \equiv -\operatorname{covar}(\boldsymbol{u}^{\bullet}, c) \equiv \int_{v_f} \boldsymbol{u}^{\bullet} \, dv_f \int_{v_f} c \, dv_f - \int_{v_f} \boldsymbol{u}^{\bullet} c \, dv_f = (\boldsymbol{u}_s / \varepsilon) \langle c \rangle - \langle \boldsymbol{u}^{\bullet} c \rangle$$
 (7)

Here, v_f is the interstitial fluid volume occupied by electrolyte. Further, once $\langle \pmb{w} \rangle$ is known we posit that the average advective-flux can be used directly as a kind of *constitutive* equation within local volume-averaged or macro-homogeneous formulations by

⁴ We note that $\bar{c}_s/(\partial \bar{c}/\partial n)|_s$ has previously been referred to as the diffusion impedance under potential modulation [41,77], and it can be obtained from the reciprocal of the gradient transfer function G as $G(\omega,r) \equiv -1/b \left[(\partial \bar{c}/\partial n)|_s/\bar{c}_s \right]$.

recognizing that $\langle \boldsymbol{u}^{\blacksquare} c \rangle = \frac{u_s}{\varepsilon} \langle c \rangle - \langle \boldsymbol{W} \rangle$, which is an alternative to the common assumption of $\langle \boldsymbol{u}^{\blacksquare} c \rangle = \frac{u_s}{\varepsilon} \langle c \rangle$ that is valid only when $covar(\boldsymbol{u}^{\blacksquare}, c) = 0$.

The utility of $\langle W \rangle$ in volume-averaged formulations motivates predicting its response to transient impulses. In the spirit of modeling such effects subject to arbitrary variations of interfacial conditions, we define a corresponding *advective-flux transfer function* $\langle N \rangle$ in terms of $\langle \overline{W} \rangle$ and $\Delta \bar{c} = \bar{c}_s - \langle \bar{c} \rangle$.

$$\langle N \rangle \equiv \frac{\varepsilon}{|u_{S}|} \frac{\langle \overline{W} \rangle}{\bar{c}_{S} - \langle \bar{c} \rangle} \tag{8}$$

Analysis of Eq. 7 shows that $\langle W \rangle$ scales in proportion to the characteristic interstitial velocity u_s/ε . Thus, we normalize $\langle N \rangle$ by $|u_s|/\varepsilon$, and we decompose it into streamwise $(\langle N \rangle_{\parallel} = \langle N \rangle \cdot \hat{e}_{\parallel})$ and transverse $(\langle N \rangle_{\perp} = \langle N \rangle \cdot \hat{e}_{\perp})$ components, where \hat{e}_{\parallel} and \hat{e}_{\perp} are streamwise and transverse unit vectors with respect to u_s :

$$\langle N \rangle_{\parallel}(\omega) \equiv \frac{\langle \overline{w} \rangle_{\parallel}}{\frac{|u_{S}|}{\varepsilon} \left[\overline{c_{S}} - \langle \overline{c} \rangle \right]} = \frac{\langle \mathbb{C} \rangle}{1 - \langle \mathbb{C} \rangle} - \left(\frac{\varepsilon}{|u_{S}|} \right) \frac{\langle u_{\parallel}^{\bullet} \mathbb{C} \rangle}{1 - \langle \mathbb{C} \rangle}$$
(9a)

$$\langle N \rangle_{\perp}(\omega) \equiv \frac{\langle \overline{w} \rangle_{\perp}}{\frac{|u_{S}|}{\varepsilon} \left[\overline{c}_{S} - \langle \overline{c} \rangle\right]} = -\left(\frac{\varepsilon}{|u_{S}|}\right) \frac{\langle u_{\perp}^{\bullet} \mathbb{C} \rangle}{1 - \langle \mathbb{C} \rangle} \tag{9b}$$

We note that $\langle N \rangle_{\parallel}$ and $\langle N \rangle_{\perp}$ are respectively expressed in terms of pore-scale velocity components that are parallel $u_{\parallel}^{\blacksquare}$ and transverse u_{\perp}^{\blacksquare} to the superficial velocity vector \boldsymbol{u}_s . While Eq. 9 alone is sufficient to capture the vectorial nature of $\langle \boldsymbol{N} \rangle$ in two-dimensional systems, in practice two distinct $\langle N \rangle_{\perp}$ components would be needed along orthogonal directions to capture such effects for three-dimensional systems. With $\langle N \rangle_j$ known along each direction j the corresponding component of average advective flux $\langle \boldsymbol{u}^{\blacksquare} c \rangle \cdot \hat{\boldsymbol{e}}_j$ can be determined in the time domain as $\langle \boldsymbol{u}^{\blacksquare} c \rangle \cdot \hat{\boldsymbol{e}}_j = (1/\varepsilon) \big[(\boldsymbol{u}_s \cdot \hat{\boldsymbol{e}}_j) \langle c \rangle - |\boldsymbol{u}_s| \mathcal{F}^{-1} \big\{ \langle N \rangle_j (\bar{c}_s - \langle \bar{c} \rangle) \big\} \big]$.

2.2. Macro-scale time-domain governing equations

Here we present governing equations for the macro-scale transport of redox-active species using porous electrode theory. In such a formulation the porous electrode is considered as a superposition of two continua, one representing the liquid phase and the other representing the solid phase, where spatially varying quantities are included using their volume averaged values. While a dearth of past work using porous electrode theory has been done, we refer interested readers to the seminal work where its basic postulates were first presented [58]. We first express a macroscopic mass balance equation by embedding the TFs $\langle \widehat{Sh} \rangle$ and $\langle N \rangle$ to account for their time-dependent production/consumption rates and enhanced/retarded advection rates due to their transient redox at interfaces. As both TFs are obtained in the frequency domain, their inverse Fourier transforms are taken and implemented in a consistent manner. Further, we neglect the macro-scale diffusion of reactive species by considering negligible concentration variation across the reactor lengths parallel and perpendicular to the

macroscopic flow direction. In the limit of vanishing macro-scale diffusion, the up-scaled mass conservation for species i can be expressed in terms of the macroscopic volume averaged concentration $\langle c_i \rangle$ as:

$$\varepsilon \frac{\partial \langle c_i \rangle}{\partial t} + \nabla \cdot \boldsymbol{u}_s \langle c_i \rangle - |\boldsymbol{u}_s| \nabla \cdot \mathcal{F}^{-1} \{ \langle \boldsymbol{N} \rangle (\bar{c}_{s,i} - \langle \bar{c} \rangle_i) \} = \frac{aD_i}{s,b} \mathcal{F}^{-1} \{ \langle \widetilde{Sh} \rangle (\bar{c}_{s,i} - \langle \bar{c} \rangle_i) \}$$
(10)

Here, $\langle c_i \rangle (r,t)$ is local volume-averaged concentration obtained by averaging c_i over a finite volume larger than a periodic unit representing the porous microstructure. The source term at the right-hand side of Eq. 10 accounts for the transient volumetric production/consumption rate of species that is coupled to the transient current density $\langle i \rangle_s$ as $a\langle i \rangle_s/(s_iF) = (a)\langle j_i \rangle_s = aD/(s_ib)~\mathcal{F}^{-1}\{\langle \widetilde{Sh}\rangle (\bar{c}_{s,i} - \langle \bar{c}\rangle_i)\}$. Further, the term $|u_s| \nabla \cdot \mathcal{F}^{-1}\{\langle N\rangle (\bar{c}_{s,i} - \langle \bar{c}\rangle_i)\}$ accounts for the deviation (acceleration/suppression) in reactive species advection rate through the porous electrode. We modeled the reaction at the solid/solution interface by using Butler-Volmer (B-V) kinetics (Eq. 11), which describes the current-overpotential relationship considering symmetric reaction kinetics for both oxidation and reduction:

$$i = i_0 \left[exp\left(\frac{F\eta}{2RT}\right) - exp\left(-\frac{F\eta}{2RT}\right) \right] \tag{11}$$

Here, i is the current density at the electrode surface, i_0 is the exchange current density, and RT/F is the thermal voltage. The reaction overpotential η is expressed using the solid phase potential ϕ_s , solution (electrolyte) phase potential ϕ_e , and the equilibrium potential ϕ_{eq} as:

$$\eta = \phi_s - \phi_e - \phi_{eq} = \phi_s - \phi_e - \left(\frac{RT}{F}\right) ln\left(\frac{c_{O,s}}{c_{R,s}}\right)$$
(12)

Further, the mass conservation equation for a well-mixed tank without any consumption/production of species is expressed by Eq. 13, where $\langle c_i \rangle^T$ is the volume averaged concentration of species i inside the tank.

$$\frac{\partial \langle c_i \rangle^T}{\partial t} + \nabla \cdot \boldsymbol{u}_S \langle c_i \rangle^T = 0 \tag{13}$$

The assumption well-mixed refers to the fact that the local concentration field inside the tank is uniform.

3. Experimental validation of bottom-up transient model

In this section we compare model predictions based on Section 2 with experimental results obtained from the transient response of an electrolyte solution containing the $Fe(CN)_6^{4-}/Fe(CN)_6^{3-}$ couple at 50% state-of-charge that undergoes reversible redox via $Fe(CN)_6^{3-} + e^- \leftrightharpoons Fe(CN)_6^{4-}$. This redox couple was chosen for its facile reaction kinetics (rate constant of $k_s = 0.1 \sim 1 \ cm/s$ [59–62]), so as to produce negligible kinetic overpotential in the present experiments. The experimental reactor consisted of two graphite foil electrodes (Ceramaterials) laser-engraved (Trotec Speedy

Flexx 400 fiber laser) with ~100 μ m wide parallel microchannels that were separated by a non-selective separator (NP030 from STERLITECH Corporation). Electrolyte containing 15 mM active species and 3 M KCl supporting salt was pumped through the microchannels in the electrodes. To probe the electrodes' transient response current was applied using a square wave with half-period or pulse-width τ , as shown in Fig. D2b. Experimental methods and model implementation are provided in the supplementary information.

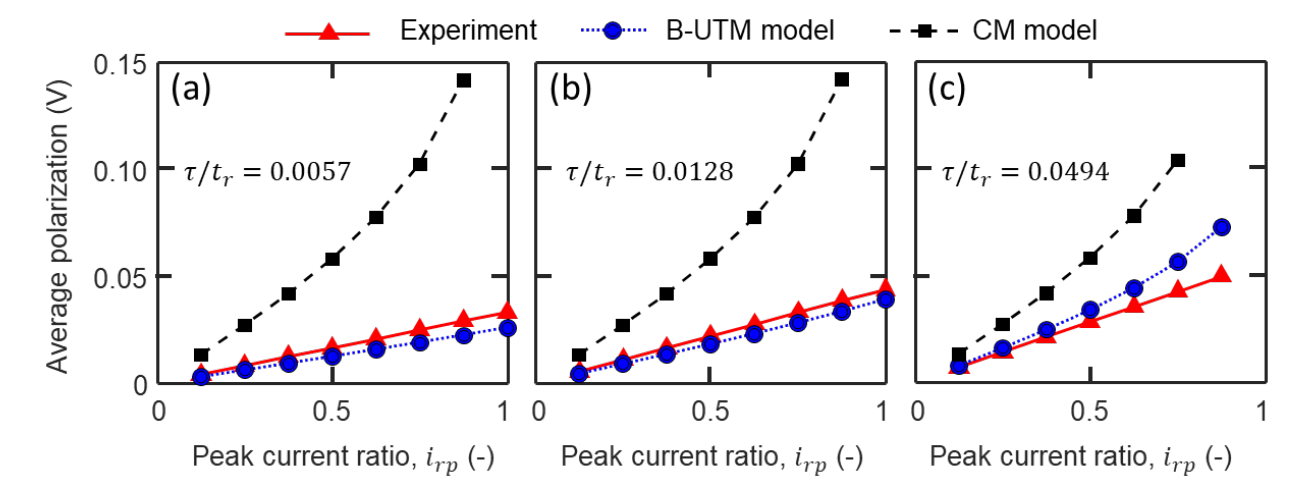


Fig. 2: Variation of average concentration polarization with applied current ratio i_{rp} at different pulse width τ . (a) $\tau/t_r = 0.0057$, (b) $\tau/t_r = 0.0128$ and (c) $\tau/t_r = 0.0494$. t_r is the mean residence time of solute $(t_r = L_r/u_s)$.

Figure D3 in the supplementary information shows the time variation of IRcorrected cell voltage with non-dimensional time. In contrast with our experimental results, the conventional model (CM) – that uses a time-invariant film law of mass transfer and that neglects solution advection suppression/acceleration - shows instantaneous jumps in polarization when applied current is switched with a sufficiently small pulse width (τ < 10). On the contrary the present bottom-up transient model (B-UTM) captures the dynamic response in good agreement with experiment for such pulse widths, the deviations of which arise from the statistical distribution of electrode cross-section area and the uncertainty active-species diffusivity. For such short pulses diffusion is inherently transient with concentration variations penetrating from interfaces into bulk to an extent that is much shorter than the characteristic pore dimension (~100 µm), thus validating the transient aspects of the present B-UTM model. For large impulse duration ($\tau \geq 10$) where solute transport occurs through the entirety of pores, we observe that both the CM and B-UTM models produce polarization variation with time that deviates qualitatively from experiment, likely as a result of factors that both models neglect including entrance region effects and macroscopic diffusion, dispersion, and ion conduction. Despite this, we note that B-UTM shows less deviation from experiment than CM. We attribute this outcome for B-UTM to its accounting of the suppression/acceleration arising from the

inhomogeneity of pore scale concentration and velocity fields, validating its inclusion in the present model.

Modeled and experimental time-averaged polarization for the various conditions tested are shown in Fig. 2. The experimental data shows that average polarization depends not only on the applied peak current ratio i_{rp} , but also on the pulse duration τ . The CM model fails to capture the dependence of average polarization on impulse duration τ . Further, this inability to capture transient response causes CM prediction to deviate substantially at high current ratio where it over-predicts the polarization up to 400%, and it prevents such models from simulating RFBs with near-limiting ($i_{rp} \sim 1$) and over-limiting ($i_{rp} > 1$) conditions that have been observed in previous studies [63–67]. On the other hand, the present B-UTM model is not only capable of simulating the near-limiting and over-limiting operations, but it also produces more accurate predictions at all i_{rp} and τ values tested.

4. Pore-scale simulations versus frequency

Using the frequency-based theory introduced in Sec. 2.1, we obtained results for numerical simulations performed by applying that theory to study the transient response of redox-active electrolyte flowing through a porous electrode comprised of infinite cylinders undergoing crossflow as a representative geometry for carbon fiber felt commonly used in RFBs. Here, pore-scale simulation results are presented to show the characteristics of the frequency-dependent TFs. These simulations are used to investigate the effect of microstructure porosity, superficial velocity, and frequency, where different cases are created by varying their corresponding non-dimensional parameters to make the results extensible to other conditions, provided that geometric, hydrodynamic, and mass-transfer similarity criteria are satisfied. The non-dimensional frequency $f^* \equiv$ $\omega b^2/2\pi D$ is the ratio of the characteristic time-scale for diffusion $(\tau_d=b^2/D)$ to the time-scale associated with the angular frequency ω $(\tau_{c/d}=2\pi/\omega)$. For $f^*\ll 1$ we find that pore-scale mass transfer is consistent with that of the pseudo-steady limit, while higher frequencies produce a finite temporal lag in response that we show is a signature of transient response. For the present simulations we choose the characteristic length b as the cylinder diameter d. Subsequently, we present results for the local-concentration transfer function $\mathbb{C}(\omega, \mathbf{r})$, the overall spectral Sherwood number $\langle \widetilde{Sh} \rangle(\omega)$, and the parallel/transverse components of the average advective-flux transfer function $\langle N \rangle_{\parallel/\perp}(\omega)$.

We solved the transformed MCE (Eq. 4) numerically in the frequency domain to obtain $\mathbb{C}(\omega,r)$ for a two-dimensional porous microstructure. The porous electrodes investigated here are regular arrays of unconsolidated cylinders of infinite length and diameter d (Fig. 3a). Simulations were performed over a domain defined by the unit cell shown in Fig. 3b and 3c. We present simulated results for the transient response of solution within microstructures having $\varepsilon=0.546$ and $\varepsilon=0.874$ as representative cases in the limits of low and high porosity respectively. Inline flow with superficial velocity u_s parallel to the x-axis was simulated with Pe ranging from 10^{-2} to 22.8×10^3 .

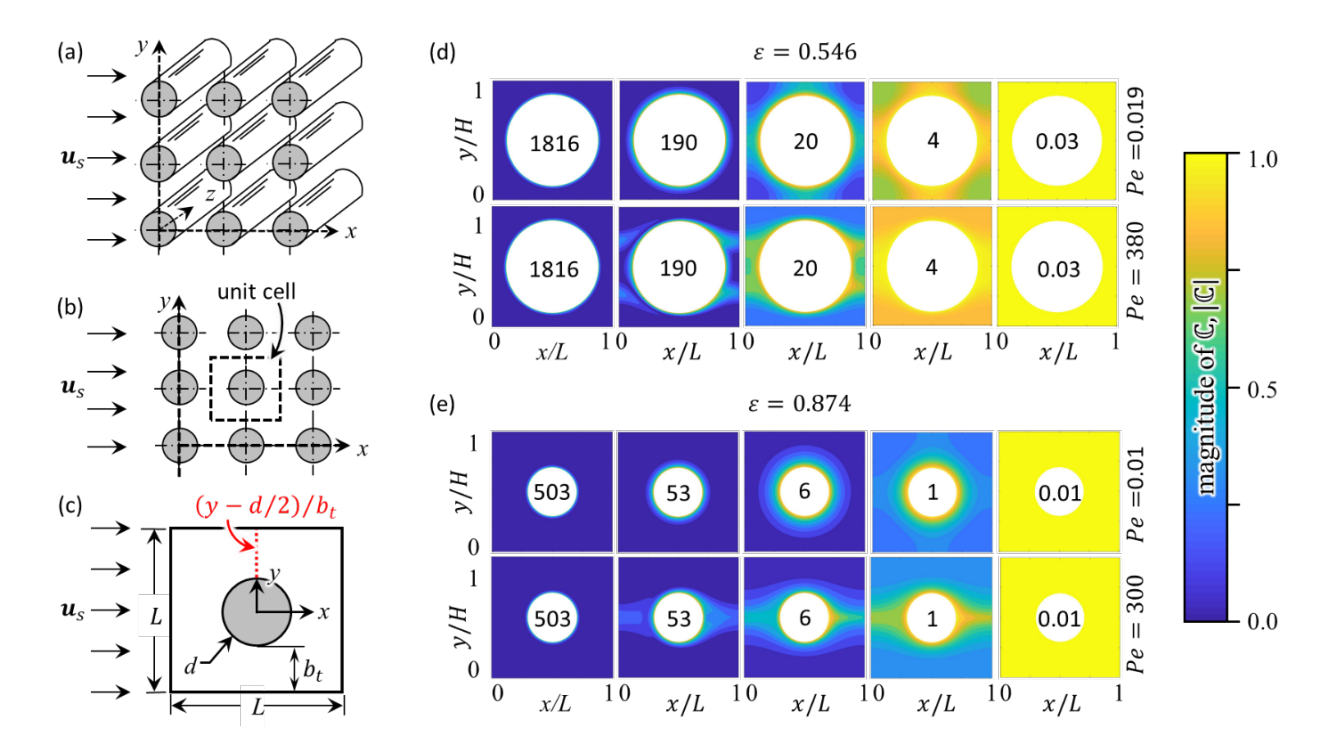


Fig. 3. Schematic of the modeled periodic domain: (a) regular, unconsolidated array of infinite circular cylinders with bulk electrolyte flow through interstitial pores, (b) designation of a repetitive unit cell with a circular cylinder at the cell's center, and (c) enlarged view of a repetitive unit cell annotated with dimensions. A given microstructure's porosity ε results in a certain minimum pore dimension b_t at the pore throat shown in (c). Spatial distribution of $|\mathbb{C}|$ at different nondimensional frequencies for (d) $\varepsilon=0.546$ with Pe=0.019 (first row) and Pe=380 (second row), and (e) $\varepsilon=0.874$ with Pe=0.01 (first row) and Pe=300 (second row). The bulk flow direction is horizontal from left to right. The values at the center of each distribution show the corresponding nondimensional frequency f^* .

The electrolyte solution flowing through the microstructure's pores is assumed as a Newtonian, isochoric solution with constant dynamic viscosity, while the flow field is modeled as steady, creeping flow, as justified by a small pore-scale Reynolds number: $Re = Pe/Sc \ll 1$, where Sc is Schmidt number. The pore-scale velocity field $\boldsymbol{u}^{\blacksquare}$ is obtained from numerical solution of a time-independent, inertia-free version of the vorticity transport equation (VTE) that is written in terms of the stream function ψ as $\nabla^4\psi=0$ [68]. The VTE is solved with appropriate BCs imposed on cylinder surfaces (i.e., no-slip, impermeability, and no-lift) and at the unit-cell boundaries (i.e., periodic jump/fall). For a finite frequency ($\omega>0$) the corresponding $\mathbb{C}(\omega,\boldsymbol{r})$ field is obtained by solving Eq. 4 with periodic BCs applied at unit-cell boundaries, along with a Dirichlet BC $\mathbb{C}_s=1$ at cylinder surfaces. Details of discretization, numerical implementation, and model verification are shown in the supplementary information.

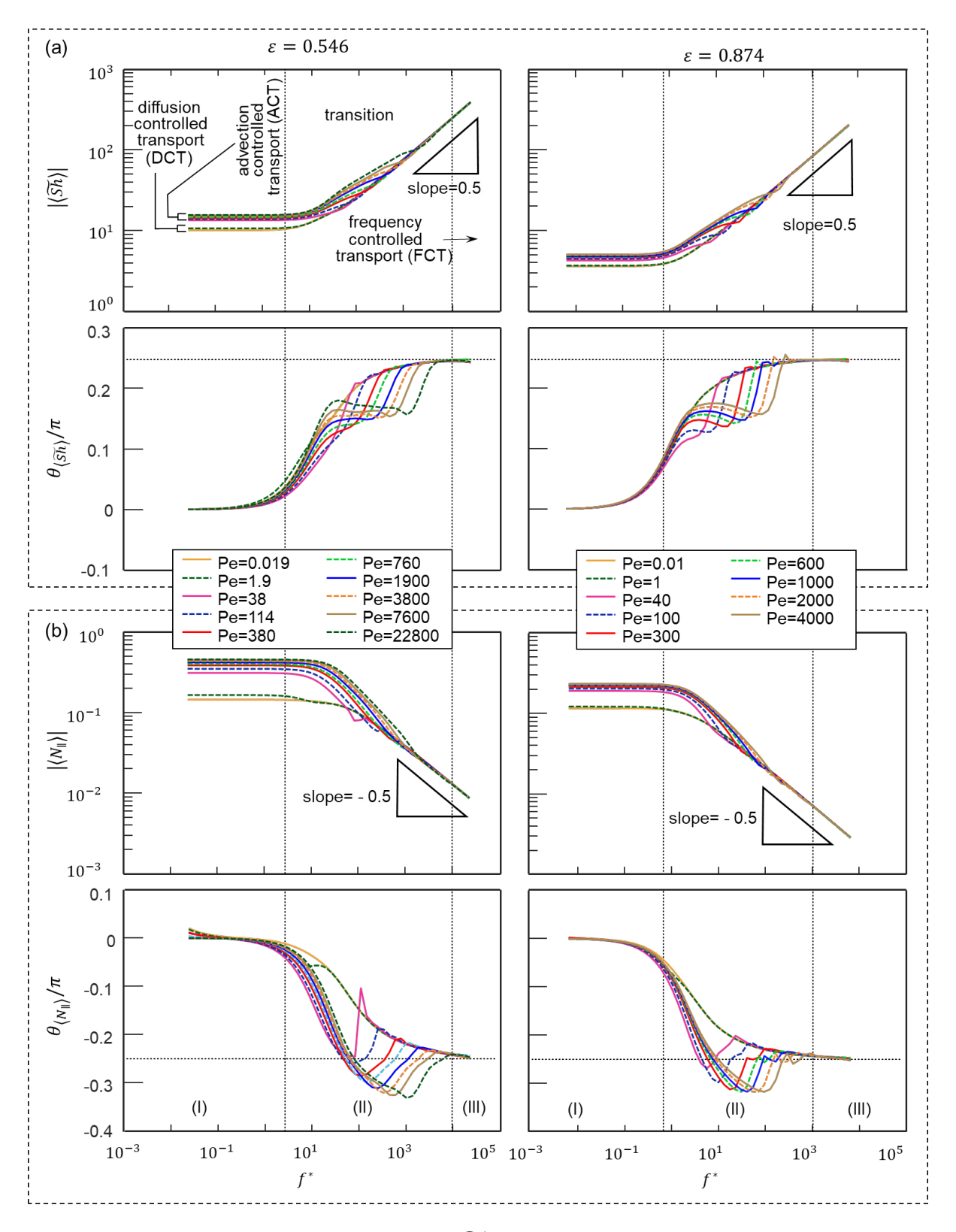


Fig. 4. Variation of transfer functions (a) $\langle\widetilde{Sh}\rangle$ and (b) $\langle N\rangle_{\parallel}$ with frequency for $\varepsilon=0.546$ (left panel) and $\varepsilon=0.874$ (right panel). The upper and lower row show magnitude and phase of the respective TFs.

4.1. Concentration

Figures 3d and 3e show the spatial distribution of $|\mathbb{C}| = \sqrt{(\mathrm{Re}[\mathbb{C}])^2 + (\mathrm{Im}[\mathbb{C}])^2}$ as a function of non-dimensional frequency for high and low porosity values with either high or low Péclet number. At sufficiently high frequency $(f^* \gg 200)$ these distributions reveal that most solution volume remains unaffected by the disturbance induced by interfacial reactions for all Pe and ε studied and that variations of $|\mathbb{C}|$ are focused near solid/solution interfaces. This effect is caused by the comparatively slow rate of diffusion relative to the frequency at which the surface concentration is cycled in such a limit. As a result, the disturbance occurring at the solid/solution interface is unable to propagate substantially into bulk solution before a new cycle of concentration fluctuation starts at the interface.

When the characteristic diffusion time-scale is comparable with the time-scale for cycling at the solid/solution interface ($f^*=1{\sim}200$), $|\mathbb{C}|$ varies in space in different ways depending on what the predominant mass-transfer mode is. For $Pe \ll 1$, the spatial distribution of $|\mathbb{C}|$ is symmetric with respect to the x and y axes, and $|\mathbb{C}|$ approaches an axisymmetric distribution for high-porosity electrodes due to the weak interactions between adjacent cylinders. For low-porosity electrodes a four-peaked distribution is observed as a result of strong inter-cylinder interactions that are evidenced by peak positions coinciding with the surface positions at which neighboring cylinders have closest proximity. For high Pe cases the spatial distribution of $|\mathbb{C}|$ becomes skewed along the streamwise direction as a result of the predominant role of advection mass transfer in that limit. In the limit of vanishing frequency ($f^* \ll 1$) the distribution of $|\mathbb{C}|$ approaches a uniform value of unity (i.e., $|\mathbb{C}|=1$) as a result of the lagless tracking of surface concentration by the entire concentration field in that limit. However, we note that such an attribute does not imply an infinite mass transfer coefficient, as evidenced by our subsequent investigation of the spectral Sherwood number.

In the pseudo-steady limit our previous simulations revealed that the effect of advective mass transport is evidenced by the shape of the concentration profile at the midplane of the cylinder and along the direction transverse to the streamwise direction [38]. To determine how frequency influences such profiles the non-dimensional concentration profiles are shown in the supplementary information, and they suggest that response in the low-frequency limit is controlled primarily by the dominant transport mechanism in the solution's bulk (*pseudo-steady* diffusion and/or advection), while response in the high-frequency limit is controlled by *transient diffusion* through boundary layers of solution that exhibit frequency-specific thickness adjacent to interfaces.

4.2. Spectral Sherwood number

We now present results for the overall spectral Sherwood number $\langle \widetilde{Sh} \rangle \equiv b \langle \overline{j} \rangle_s / [D(\overline{c}_s - \langle \overline{c} \rangle)]$, which relates the average surface flux due to reactions to the concentration difference that drives it in the frequency domain. Figure 4 shows the variation with frequency of $\langle \widetilde{Sh} \rangle$ magnitude and phase for different Pe and porosity values. The variation of $\langle \widetilde{Sh} \rangle$ shows three distinct regions in the frequency domain, as annotated in Fig. 4 At high frequency (Region III) the magnitude of $\langle \widetilde{Sh} \rangle$ scales in proportion to $\sqrt{\omega}$

while phase approaches $\pi/4$, consistent with the scaling expected for a semi-infinite Warburg impedance element and consistent with our observations from Figs. 3d and 3e that compact diffusion layers form in the vicinity of the solid/solution interfaces in the high-frequency limit. In this part of the frequency spectrum surface-concentration fluctuations alone control $\langle \widetilde{Sh} \rangle$, not those of average concentration. These features result in minimal effect of Pe on $\langle \widetilde{Sh} \rangle$ at high frequencies, and as a result we refer to this region as having frequency-controlled transport (FCT). We define a lower bound for this region as the frequency where phase reaches within 5% of its asymptotic value $\pi/4$, corresponding to non-dimensional frequencies of $f^* = 10^4$ and 10^3 for microstructures with respective porosities of $\varepsilon = 0.546$ and 0.874.

At low frequency (Region I) the magnitude of $\langle\widetilde{Sh}\rangle$ approaches a constant non-zero value as frequency vanishes, while its phase approaches zero simultaneously. Such a limiting phase value shows that frequency response is lagless in this limit, an effect that results from the relatively fast mass transfer in comparison with the time-scale of boundary condition cycling. Hence, in this limit the dominant mode of pore-scale mass transfer, not the driving frequency, determines the magnitude of $\langle\widetilde{Sh}\rangle$. In this limit systems with $Pe\ll 1$ experience diffusion-controlled transport (DCT), and systems with $Pe\gg 1$ experience advection-controlled transport (ACT), consistent with our previous modeling [38] in the pseudo-steady limit. We define the upper bound for this region of the frequency domain as the lowest frequency that exhibits a value of $\langle\widetilde{Sh}\rangle$ that is 5% higher than its value in the pseudo-steady limit, corresponding to non-dimensional frequencies of $f^*=3.4$ and 0.8 for microstructures with respective porosities of $\varepsilon=0.546$ and 0.874.

In between Regions I and III, we observe Pe-specific transitions from low to high frequency (Region II) as a result of the characteristic diffusion time-scale being comparable to the time period of boundary cycling. Within this region the magnitude and the phase of $\langle \widetilde{Sh} \rangle$ show frequency dependence that is distinguishable for different extremes of Péclet number. For systems with low Péclet number ($Pe \ll 1$) a smooth, monotonic variation of phase is observed with frequency as a result of its transition from diffusion-controlled transport at low frequency to frequency-controlled transport at high frequency. On the other hand, for systems with high Péclet number ($Pe \gg 1$) the variation of phase with frequency is non-monotonic because of its transition from advection-controlled transport to frequency-controlled transport.

4.3. Advective-flux transfer function

Solute can either deplete or accumulate adjacent to such interfaces due to the finite reaction rates occurring at solid/solution interfaces, thus reducing the effectiveness of advective transport near such interfaces because of the no-slip condition. To characterize such effects, in Sec. 2.1.2.3 we introduced a non-dimensional advective-flux transfer function $\langle N \rangle \equiv -\text{covar}(\boldsymbol{u}^{\bullet}, \bar{c}) \varepsilon/[|\boldsymbol{u}_{s}|(\bar{c}_{s} - \langle \bar{c} \rangle)]$ that quantifies the departure $covar(\boldsymbol{u}^{\bullet}, \bar{c})$ of average advective-flux $\langle \boldsymbol{u}^{\bullet}\bar{c} \rangle$ in the frequency domain from its value $\langle \boldsymbol{u}^{\bullet}\rangle\langle\bar{c}\rangle$ that is expected for homogeneous concentration and velocity fields. When a microstructure comprised of a square array of cylinders is subjected to horizontal flow along the x-axis, velocity and concentration fields are produced that show reflection

symmetry about a line directed in the streamwise direction that also passes through the cylinder's centroid. For such cases to which we restrict the present investigation, the transverse component of $\langle N \rangle$ is identically zero by virtue of this symmetry. Thus, in Fig. 4b we present simulated results for the variation with frequency of the streamwise component of $\langle N \rangle$ at different Pe and porosity values, denoted as $\langle N \rangle_{\parallel}$.

At high frequencies, $|\langle N \rangle_{\parallel}|$ decreases with increasing frequency by following a power law correlation with exponent -0.5, while a negligible effect of Pe is observed because of frequency-controlled transport in that limit. The decrease in $|\langle N \rangle_{\parallel}|$ with increasing frequency can be attributed to the fact that the steep concentration gradients that are produced at interfaces at high frequency (Figs. 3c and 3d) promote supply of reactant as well as the removal of product. In this frequency region the phase of $\langle N \rangle_{\parallel}$ approaches $-\pi/4$. At low frequencies the magnitude of $\langle N \rangle_{\parallel}$ approaches a constant, non-zero value that depends on porosity, while its phase approaches zero, consistent with the lagless response that is a hallmark of the pseudo-steady limit. Similar to our observations for $\langle \widehat{Sh} \rangle$, $\langle N \rangle_{\parallel}$ shows smooth, monotonic variation for the transition from diffusion-controlled transport to frequency-controlled transport at low Péclet number $(Pe \ll 1)$, while non-monotonic variation is apparent for the transition from advection-controlled transport to frequency-controlled transport at high Péclet number $(Pe \gg 200)$.

5. Macro-scale simulations versus time

Here we present simulations of the macro-scale response of an RFB subjected to step impulse current variation by solving the TF embedded macro-scale MCEs from Sec. 2.2 (Eqs. 10-13) in the time domain. We assume that an ideal separator isolates the highand low-potential sides of its reactor to eliminate crossover of reactive species. Thus, we limit our study to one side of the reactor (i.e., a half cell) where a reduced species R is oxidized to produce O due to a positive current applied at solution/electrode interfaces. Assuming a parallel flow configuration and assuming negligible macro-scale concentration gradients in the transverse direction, a one-dimensional model is sufficient to capture the temporal and spatial variation of $\langle c_i \rangle$ along the reactor's length L_r (Fig. 5b). We discretized each electrode into 50 finite volumes (FVs) over which the local concentrations are averaged to obtain $\langle c_i \rangle$ (see Fig. 5b). Each tank was represented by a single FV with a time-dependent average concentration $(c_i)^T$. The step impulse variation of the applied current is presented non-dimensionally by defining a current ratio i_r where the applied current density i_{app} is normalized by the limiting current density i_{lim} . The limiting current density is calculated as $i_{lim} = FD\langle c_R \rangle^{ini} \langle Sh \rangle / d$, where $\langle Sh \rangle$ is the timeindependent Sherwood number corresponding to PSL. The step impulse variation is created by instantaneously increasing $\emph{i}_{\emph{r}}$ to a peak-current ratio $\emph{i}_{\emph{rp}}$ (from a base current ratio $i_{rb}=0.1$) for a time au, after which i_r returns to its initial value. Both au and i_{rp} were varied to simulate different cases of RFB operation with high- ($\varepsilon = 0.874$) and low- ($\varepsilon =$ 0.546) porosity electrodes.

For all cases simulated, the nondimensional flow rate β was at least 16 to prevent reactant depletion at the reactive interface due to insufficient electrolyte flow [69]. Here, β is the actual flow rate Q_{actual} normalized by the stoichiometric flow rate Q_{stoic} , where

 $Q_{stoic} = (V_{tank} + V_{reactor})/ au_{th}$ depends on the electrolyte volume in the tank (V_{tank}) and the reactor $(V_{reactor})$ and on the theoretical charging/discharging time au_{th} , resulting in a certain Péclet number for low $(Pe = 22.8 \times 10^3)$ and high $(Pe = 4 \times 10^3)$ porosity electrodes using $Pe = Q_{actual}d/A_rD$. In practice, au_{th} was determined by Faradaic balance from the theoretical charge-storage capacity of the redox-active electrolyte and the magnitude of the applied current. A kinetic rate constant that produces a Damköhler number of 414 (Da = kd/D) was used to ensure that reaction polarization was negligible compared to the concentration polarization. For all cases the tank and the reactor were initialized with identical electrolyte solution comprised of 90.9% reactant (R) and 9.1% product (O) and were charged for 160 seconds with $i_{rb} = 0.1$ before the step impulse was applied. The time ranges presented were adjusted so that the step-impulse current started at t = 0.

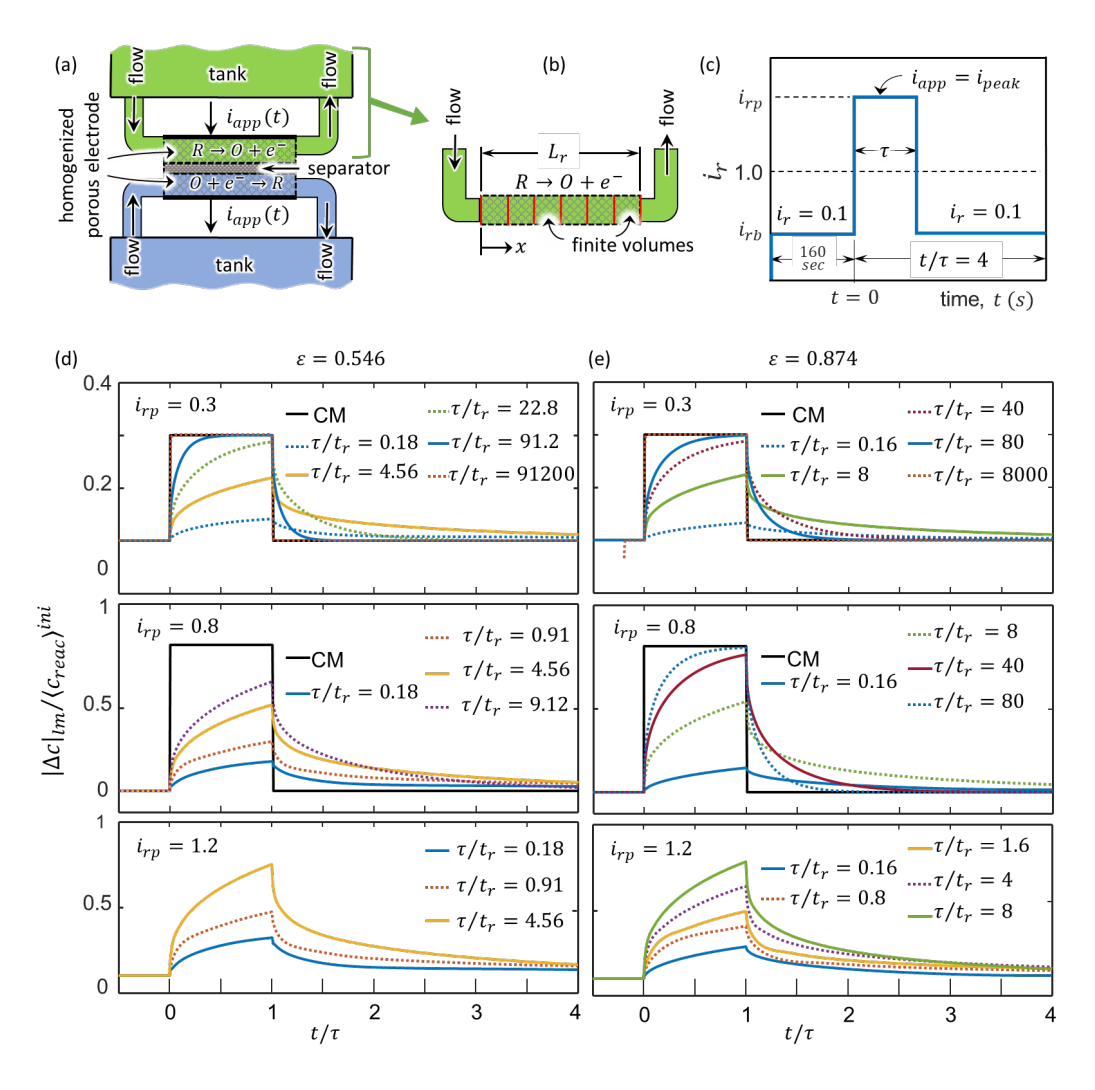


Fig. 5. (a) Schematic of an RFB with electrolyte flowing through both sides of the reactor, (b) one-dimensional model showing the upper half cell with finite volumes, and (c) step impulse variation of applied current density with time shown as current ratio i_r . Variation of maximum local concentration polarization $|\Delta c|_{lm}$ with time at different τ/t_r for (d) $\varepsilon=0.546$ and (e) $\varepsilon=0.874$.

We used a self-consistent iterative algorithm to solve Eqs. 10-13 numerically, where $\langle c_i \rangle$ and $\langle c_i \rangle^T$ were calculated from the discretized mass conservation equations written for each FV inside the reactor (Eq. 10) and the tank (Eq. 13). The inverse Fourier transforms appearing in Eq. 10 were calculated using a state-space model for each TF by recognizing that the system is linear time-invariant [39,70]: $\langle TF \rangle = C(j\omega I - A)^{-1}B + D$, where $\langle TF \rangle$ is a rational approximation to a given irrational TF and A,B,C, and D are system matrices/vectors. Since $\langle \widetilde{Sh} \rangle$ is an improper transfer function due to its divergence at infinite frequency (see Fig. 4a), we determined a state-space model for its reciprocal $\langle \widetilde{Z} \rangle = 1/\langle \widetilde{Sh} \rangle$. To obtain the poles p_i and residues r_i for rational approximations to $\langle \widetilde{Z} \rangle$ and $\langle N_{\parallel} \rangle$, a vector-fitting algorithm was used [71–73]. Additional details of the model's discretization, self-consistent iterative algorithm, state-space models, vector fitting, and verification are included in the supplementary information.

5.1. Concentration polarization across electrode pores

We used the macro-scale numerical model to analyze the transient concentration polarization inside of the RFB reactor. The corresponding time variation of local maximum concentration polarization $|\Delta c|_{lm}(t) = max(|c_{i,s}(t) - \langle c_i \rangle (r,t)|)$ is shown in Fig. 6 for different porosity ε , peak-current ratio i_{rn} , and impulse duration τ values. We focus on $|\Delta c|_{lm}$ because the reactor is most likely to deplete where and when $|\Delta c|$ is maximum. Numerical solutions were also obtained assuming time-independent $\langle Sh \rangle$ and negligible solute acceleration/suppression (i.e., $\langle N \rangle = 0$) as a conventional model (CM) against which to benchmark the present bottom-up transient model (B-UTM). For all cases studied in this section, advection is the dominant mode of transport because $Pe \gg 1$ was chosen. As we subsequently show, the dynamic response of such systems is dictated by (i) the characteristic time-scale of the transient input and (ii) the average time solute spends inside of the reactor. Hence, different cases of impulse duration are characterized by their corresponding τ/t_r values, where t_r is the fluid's mean residence time defined by $t_r = L_r/|u_s^{\bullet}|$. Further, we present system response versus t/τ , which represents time as a fraction of impulse duration. Fig. 6 shows that the CM model always predicts a lagless response, as evidenced by a rectangular impulse variation of $|\Delta c|_{lm}$ synchronously with the applied current.

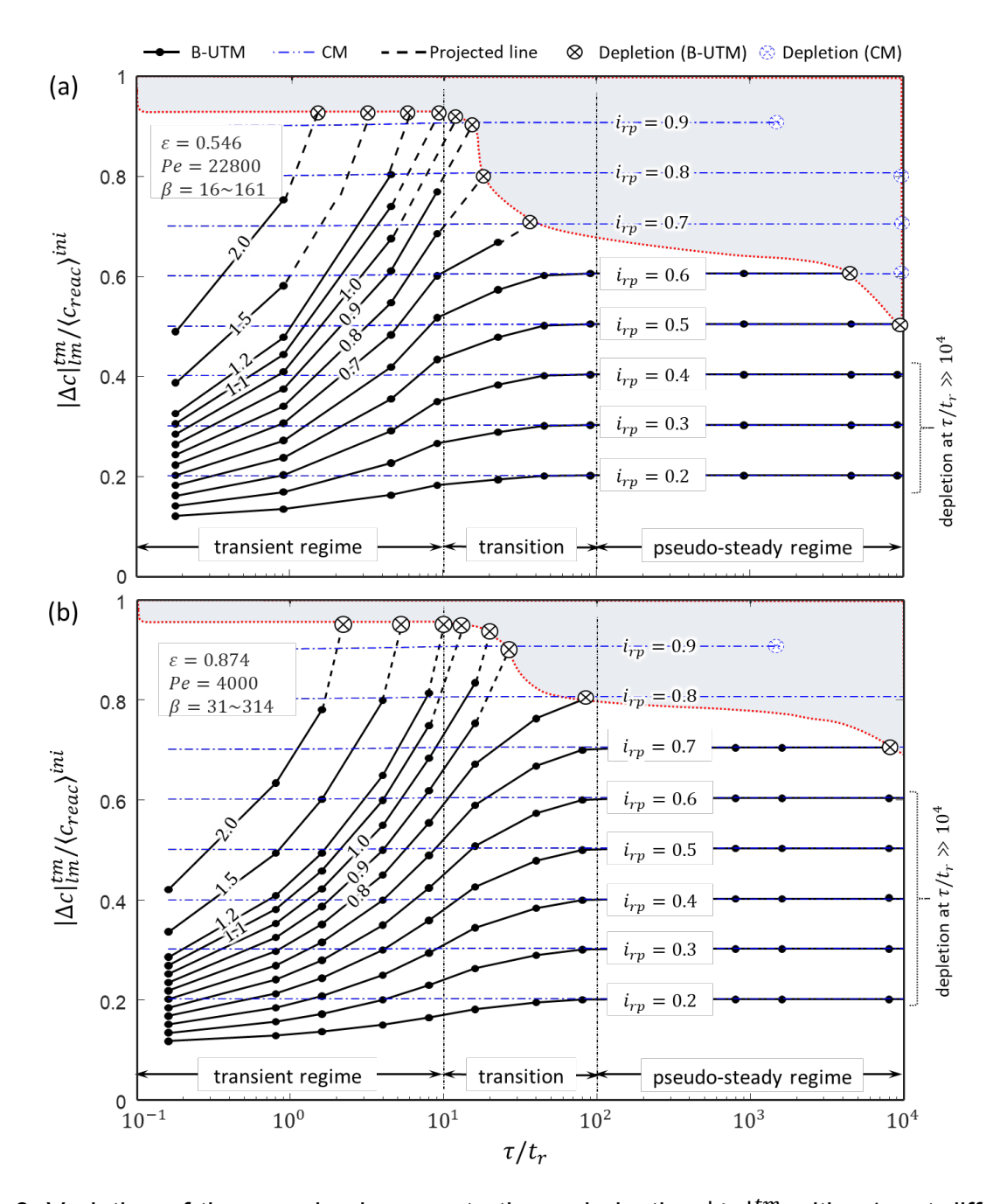


Fig. 6. Variation of time-maximal concentration polarization $|\Delta c|_{lm}^{tm}$ with τ/t_r at different peak-current ratio values i_{rp} for (a) low-porosity ($\varepsilon=0.546$, Pe=22800) and (b) high-porosity ($\varepsilon=0.874$; Pe=4000) electrodes. The corresponding i_{rp} values are overlaid on each curve. CM predictions for $i_{rp}<1$ are shown as blue-dashed lines. Cases are only presented for conditions that did not produce reactant depletion at any instant and location.

Building on these results, we constructed a non-dimensional operation map that shows the maximal concentration polarization over time versus pulse duration for different peak current ratios i_{rp} (Fig. 6). Three different regimes of impulse duration are apparent.

First, for $\tau/t_r>10^2$ the B-UTM and CM models produce identical results as a result of pseudo-steady response. Further, pore-scale transport is dominated by bulk advection. This is a consequence of the fluid's average residence time being much shorter than impulse duration, resulting in each solute molecule experiencing elevated current for less than 1% of the impulse's duration. In this regime i_{rp} alone dictates concentration polarization, while further increase of τ/t_r has neglibible effect. Second, for $\tau/t_r<10$ the B-UTM varies significantly from CM as a result of frequency-controlled transport. This is a consequence of the fluid's average residence time being similar to impulse duration, resulting in each solute molecule experiencing elevated current for more than 10% of the impulse's duration. In this regime concentration polarization is dependent on both i_{rp} and τ/t_r . Of particular note is the modest concentration polarization that is achievable even under over-limiting conditions (Figs. 6a and 6b, upper left corners) despite CM predicting inoperable conditions. Third, for $10 < \tau/t_r < 10^2$ a transition regime occurs where B-UTM predictions near $\tau/t_r \approx 10$ deviate from CM, but gradually merge with CM for $\tau/t_r \to 10^2$.

This operation map also contains a regime of vanishing concentration polarization $(|\Delta c|_{lm}^{tm}/\langle c_{reac}\rangle^{ini}\approx 0)$ that corresponds to highly efficient RFB operation with uniform reaction-rate along the streamwise direction. Such operation is achieved by long duration charging/discharging with very low current density. Another regime with very high concentration polarization $(|\Delta c|_{lm}^{tm}/\langle c_{reac}\rangle^{ini}\approx 1)$ is produced for very short duration charging/discharging with high current density that results in non-uniform reaction-rate along the streamwise direction. Under such conditions cycling terminates prematurely during local reactant depletion (Figs. 6a and 6b, gray zones with boundaries marked by cross symbols). In this regime the B-UTM model predicts reactant depletion at much lower τ/t_r compared to the CM model due to the increased advection rate of the reactant from the reactor, as elucidated subsequently.

5.2. Reactant availability through electrode pores

Apart from pore-scale concentration polarization between electrode surfaces and concentrations in the bulk of electrode pores, the local volume-averaged concentration within electrode pores $\langle c_i \rangle$ exhibits macro-scale variation along the streamwise direction. Thus, the depletion of $\langle c_i \rangle$ can cause premature termination of cycling. To quantify this effect we determined the macro-scale average of solute concentration by averaging $\langle c_i \rangle$ over each electrode as $\langle \langle c_i \rangle \rangle = 1/V_r \int \langle c_i \rangle dV$, where V_r is electrode pore volume. While Fig. 7 reveals that short duration impulses $(\tau/t_r < 10)$ produce negligible temporal change in $\langle \langle c_i \rangle \rangle$ for all cases of i_{rp} both for the B-UTM and for CM, disparate responses are observed for the two models for long duration impulses $(\tau/t_r>10^2)$. For long impulses system response is lagless for both models, but the B-UTM accounts for the impact of local reaction rate on the covariance of concentration and velocity while CM neglects it. Consequently, the B-UTM model exhibits abrupt temporal changes of $\langle \langle c_i \rangle \rangle$ that track synchronously with the abrupt change in current that occurs when the current pulse begins, whereas the CM model produces less abrupt and less significant temporal changes of $\langle \langle c_i \rangle \rangle$. For the B-UTM the sudden increase in current increases concentration polarization instantly via finite $\langle \widetilde{Sh} \rangle$, which accelerates the advection rate of reactant, causing a sudden decrease in $\langle\langle c_{reac}\rangle\rangle$ via non-zero $\langle N\rangle_{\parallel}$. Similarly, increased

concentration polarization suppresses the advection rate of product, causing $\langle\langle c_{prod}\rangle\rangle$ to increase instantly. In general, we also note that the B-UTM model retains less reactant and more product compared than CM at a given instant in time as a result of the transient experienced when current is initially turned on (see supplementary information).

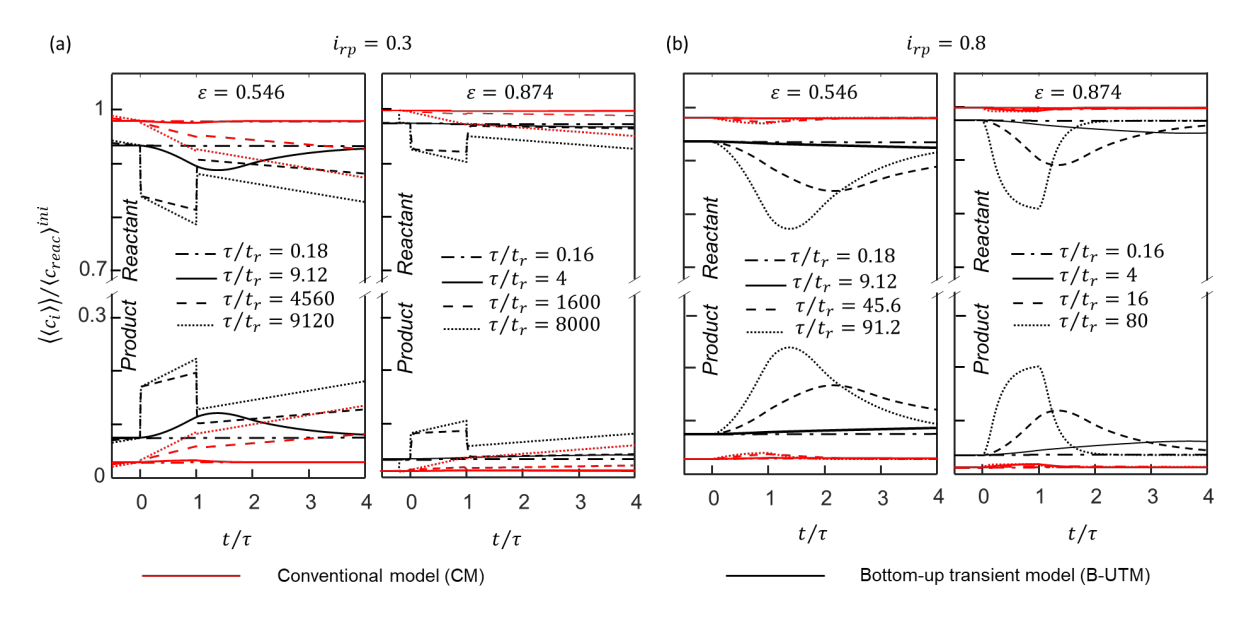


Fig. 7. Time variation of volume-averaged concentration of reactant and product $\langle\langle c_i\rangle\rangle$ for (a) $i_{rp}=0.3$ and (b) $i_{rp}=0.8$ inside an electrode of $\varepsilon=0.546$ (left panels) and $\varepsilon=0.874$ (right panels). The upper and lower half of the broken vertical axis belong to the reactant and product species respectively.

Our earlier results (Figs. 5 and 6) suggest that in the limit of short pulse duration the acceleration/suppression effect is negligible, while transient mass transport effects are substantial. The bottom-up transient model shows that such properties of the short pulse duration limit enable RFB operation with over-limiting current $(i_{rp} > 1)$. The opposite scenario is observed in the limit of long pulse duration, where the acceleration/suppression effect is significant, and the transient mass transport effect is negligible. To evaluate the relative influence of concentration polarization and reactant availability we show the variation of $\langle \langle \langle c_{reac} \rangle \rangle \rangle_t / \Delta c_{lm}^{tm}$ in Fig. 8, where $\langle \langle \langle c_{reac} \rangle \rangle \rangle_t$ is the time-averaged reactant concentration inside the reactor calculated by averaging $\langle \langle c_{reac} \rangle \rangle$ from $t/\tau=0$ to $t/\tau=4$. In the limit of short pulse duration, the B-UTM model predicts higher $\langle\langle\langle c_{reac}\rangle\rangle\rangle_t/\Delta c_{lm}^{tm}$ values compared to the CM model. The difference between B-UTM and CM in this limit is a direct result of transient mass transport effects that depends on both τ/t_r and i_r where system response is controlled by transient diffusion through the concentration boundary layer adjacent to the reactive interface. On the other hand, in the limit of long pulse duration the B-UTM produces consistently lower $\langle\langle\langle c_{reac}\rangle\rangle\rangle_t/\Delta c_{lm}^{tm}$ than CM as a result of its dominant acceleration/suppression effect. For a given peakcurrent ratio this effect remains constant in the limit of long pulse duration. Further, system response of the B-UTM in this limit is dictated either by the advection of solute by bulk electrolyte flow ($Pe \gg 1$) or by pseudo-steady diffusion across pores ($Pe \ll 1$). From Fig.

8 it is also evident that high-porosity electrodes exhibit increased transient mass transport effects and less acceleration/suppression effects compared to low-porosity electrodes. Thus, the use of high-porosity electrodes is advantageous for transient operations, along with their low pressure-drop benefits.

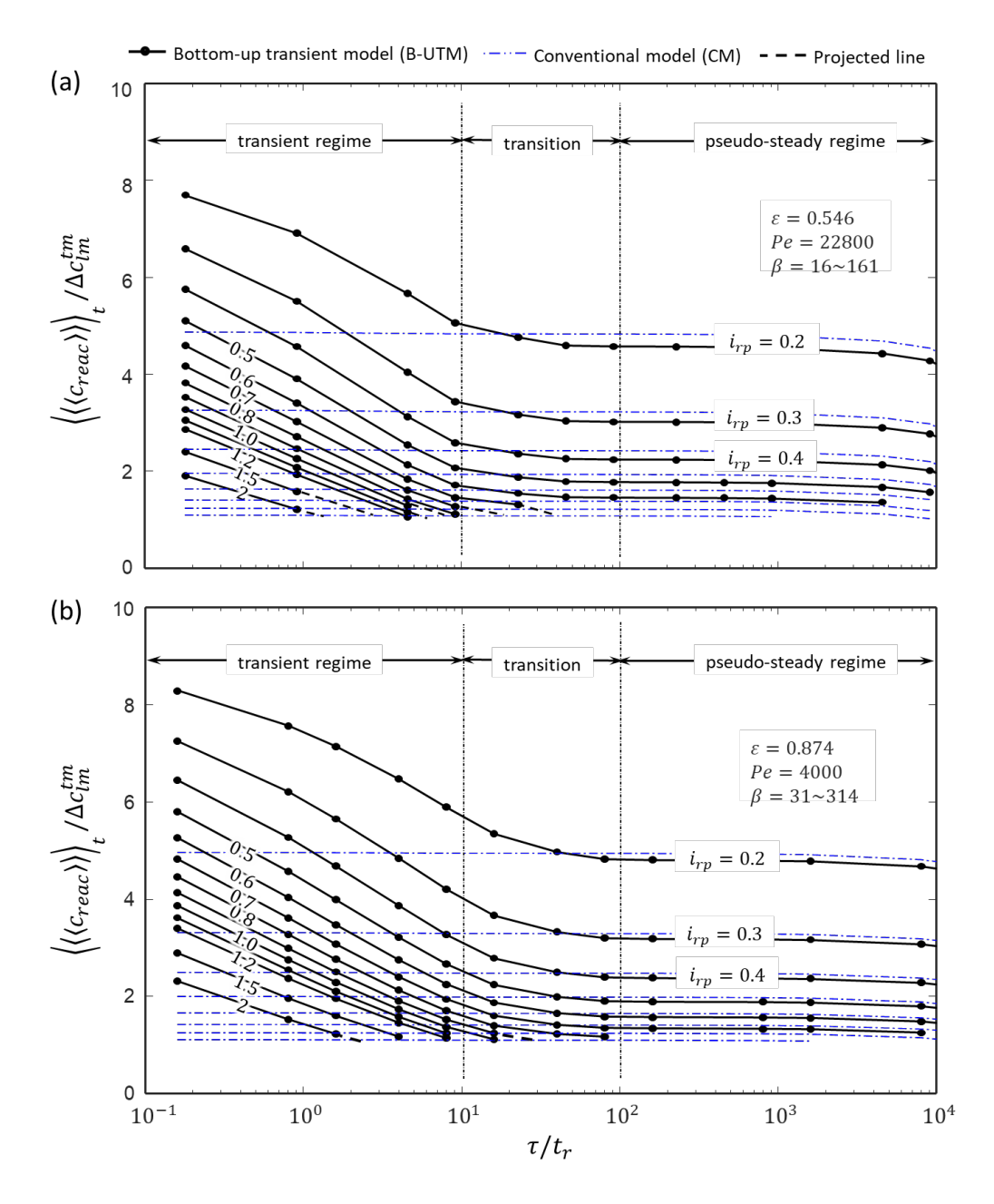


Fig. 8. Variation of time-averaged reactant concentration $\langle\langle\langle c_{reac}\rangle\rangle\rangle_t$ with τ/t_r at different peak-current ratio i_{rp} for (a) a low-porosity electrode ($\varepsilon=0.546$, Pe=22800) and (b) a high-porosity electrode ($\varepsilon=0.874$; Pe=4000). The numbers shown on the curves represent corresponding i_{rp} values. The results from CM with $i_{rp}<1$ are also shown by broken blue lines in the figures.

Conclusions

A bottom-up multi-scale modelling approach is presented to study the transient response of redox flow batteries with time-dependent current input. The transient porescale mass transport physics, including concentration polarization and the resulting deviation of advection rate of reactive species, are captured via frequency dependent transfer functions (TFs), which are incorporated into an up-scaled model through volume averaging. These transfer functions include the *spectral* Sherwood number $\langle \widetilde{Sh} \rangle$ that enables determination of the average flux on reactive surfaces $\langle j \rangle_s$ subject to a driving concentration difference at the pore-scale $\Delta c = c_s - \langle c \rangle$, as well as an advective flux transfer function $\langle N \rangle$ that captures the deviation of the total advective flux vector $\langle uc \rangle$ from its value expected in the absence of covariance between u and c (i.e., $\langle u \rangle \langle c \rangle$), subject to the same driving force Δc .

The *spectral* Sherwood number is shown for the first time to extend the conventional concept of a Sherwood number to transient conditions. Also, the advective flux transfer function describes the relative acceleration/suppression of solute advection rates relative to bulk flows, without *ad hoc* introduction of a separate velocity for solute. For solutions undergoing electrochemical reactions in porous electrodes these transfer functions provide fundamental insights into the mechanisms that could limit achievable current densities, thermodynamic efficiencies, device resilience, and cycle life. Beyond their potential significance to electrochemical systems, these concepts will also find use in understanding the coupling between reactions and convection processes in porous media, as well as in understanding transient thermal transport via formal analogies between heat and mass transfer.

Both qualitative and quantitative comparison between experiment and bottom-up transient model (B-UTM) predictions are presented in contrast with the conventional constant Sherwood number model, where the B-UTM model not only showed substantial improvement in capturing transient response, but also provides a means to simulate flow cell operations with short impulses of near-limiting and over-limiting applied current.

Aside from their future use, we demonstrated the utility of our frequency-based theory by simulating such transfer functions using a simplified microstructure containing a regular array of solid cylinders in horizontal crossflow. The effects of porous electrode microstructure, superficial velocity, and boundary cycling frequency were respectively investigated by varying porosity ε , Péclet number Pe, and nondimensional frequency f^* . From the variations of $\langle \widetilde{Sh} \rangle$ and $\langle N \rangle_{\parallel}$ with frequency at different ε and Pe we deduced three different spectral regions of response. In the low-frequency region $(f^* \ll 1)$ transport is primarily controlled by the prevailing pseudo-steady mass-transfer mode: diffusion and advection respectively for $Pe \ll 1$ and $Pe \gg 1$. In this spectral region, the magnitude of $\langle \widetilde{Sh} \rangle$ and $\langle N \rangle_{\parallel}$ approach an asymptotic non-zero value with vanishing phase lag. In the high frequency limit $(f^* \gg 1)$ transport is controlled by transient diffusion within boundary layers, showing strong dependence of each transfer function on frequency. In this spectral region, the magnitude of $\langle \widetilde{Sh} \rangle$ and $\langle N \rangle_{\parallel}$ respectively increase and decrease

according to a power law with exponent $\pm 1/2$, while their phases approach $\pm \pi/4$ in agreement with semi-infinite Warburg response.

We embedded these TFs into an up-scaled model using porous electrode theory to investigate the dynamic response of a redox flow battery operating under step impulse current input. The results obtained suggest that the dynamic response of such systems is dictated by the characteristic time-scale of transient current variation. For fast fluctuations the effect of transient mass transfer is substantial, and the system response is found to lag. For such operation significant reduction in concentration polarization is achieved with 60%-70% reduction for an applied current of 90% of the limiting current. Finally, we demonstrated that short duration charging/discharging of a redox flow battery with over-limiting current is possible, which provides a means to increase the utilization of charge capacity of existing flow-based electrochemical devices that are operated under transient conditions. Furthermore, while operating under fluctuations of low characteristic frequency, such systems reach a pseudo-steady limit with negligible transient mass transport effect. Here, the accelerated advection of reactant species from the reactor to the tank causes earlier (in time) depletion at the reactive interfaces.

These findings motivate the exploration of related effects using the presently introduced transfer functions to simulate the charging current input that is typical of renewable power sources, as well as to model such effects with different electrode microstructures. Additional physicochemical effects not shown here (e.g., macro-scale migration and diffusion of redox-active species and supporting-electrolyte ions and macro-scale superficial velocity gradients induced by the used of serpentine, interdigitated, or other flow fields) are readily coupled with the present B-UTM by adopting the two transfer functions of interest to express the interfacial redox-reaction rate and the average advection rate in place of those determined by the conventional film law of mass transfer in previous porous-electrode theory formulations of RFB models (see Ref. [24]). Further, the similarity of the time-domain governing equations motivates the use of the transfer functions defined here in other electrochemical contexts using flow-through electrodes, including electrochemical separations and energy conversion. Increased accuracy of the model is also possible by additionally including macro-scale dispersion, ion conduction, entrance region effects, and non-uniform surface concentration effects.

Acknowledgements

This research was supported by the US National Science Foundation (Award no. 1931659) and the Department of Mechanical Science and Engineering at the University of Illinois at Urbana-Champaign. We thank Irwin Loud for fabricating and characterizing the structure of the electrodes used for experimental validation that were fabricated at Siebel Center for Design, University of Illinois at Urbana-Champaign (UIUC). Structural characterization was carried out in part in the Materials Research Laboratory Central Research Facilities, UIUC. We thank Vu Do for assistance with flow-cell setup and electrochemical characterization. We thank Professor Joseph Bentsman for discussion concerning the mathematical properties of transfer functions.

REFERENCES

- [1] W. Cole, N. Gates, T. Mai, D. Greer, P. Das, 2019 Standard Scenarios Report: A U.S. Electricity Sector Outlook, Natl. Renew. Energy Lab. (2019).
- [2] W. Wang, Q. Luo, B. Li, X. Wei, L. Li, Z. Yang, Recent Progress in Redox Flow Battery Research and Development, Adv. Funct. Mater. 23 (2013) 970–986. https://doi.org/10.1002/adfm.201200694.
- [3] G.L. Soloveichik, Flow Batteries: Current Status and Trends, Chem. Rev. 115 (2015) 11533–11558. https://doi.org/10.1021/cr500720t.
- [4] Y. Matsuda, K. Tanaka, M. Okada, Y. Takasu, M. Morita, T. Matsumura-Inoue, A rechargeable redox battery utilizing ruthenium complexes with non-aqueous organic electrolyte, J. Appl. Electrochem. 18 (1988) 909–914. https://doi.org/10.1007/BF01016050.
- [5] Q. Liu, A.E.S. Sleightholme, A.A. Shinkle, Y. Li, L.T. Thompson, Non-aqueous vanadium acetylacetonate electrolyte for redox flow batteries, Electrochem. Commun. 11 (2009) 2312–2315. https://doi.org/10.1016/j.elecom.2009.10.006.
- [6] M. Yao, H. Senoh, S.I. Yamazaki, Z. Siroma, T. Sakai, K. Yasuda, High-capacity organic positive-electrode material based on a benzoquinone derivative for use in rechargeable lithium batteries, J. Power Sources. 195 (2010) 8336–8340. https://doi.org/10.1016/j.jpowsour.2010.06.069.
- [7] B. Huskinson, J. Rugolo, S.K. Mondal, M.J. Aziz, A high power density, high efficiency hydrogen-chlorine regenerative fuel cell with a low precious metal content catalyst, Energy Environ. Sci. 5 (2012) 8690–8698. https://doi.org/10.1039/c2ee22274d.
- [8] B. Sun, M. Skyllas-Kazacos, Modification of graphite electrode materials for vanadium redox flow battery application—I. Thermal treatment, Electrochim. Acta. 37 (1992) 1253–1260.
- [9] B. Sun, M. Skyllas-Kazacos, Chemical modification of graphite electrode materials for vanadium redox flow battery application-part II. Acid treatments, Electrochim. Acta. 37 (1992) 2459–2465. https://doi.org/10.1016/0013-4686(92)87084-D.
- [10] H. Kabir, I.O. Gyan, I. Francis Cheng, Electrochemical modification of a pyrolytic graphite sheet for improved negative electrode performance in the vanadium redox flow battery, J. Power Sources. 342 (2017) 31–37. https://doi.org/10.1016/j.jpowsour.2016.12.045.
- [11] H.R. Jiang, W. Shyy, M.C. Wu, R.H. Zhang, T.S. Zhao, A bi-porous graphite felt electrode with enhanced surface area and catalytic activity for vanadium redox flow batteries, Appl. Energy. 233–234 (2019) 105–113. https://doi.org/10.1016/j.apenergy.2018.10.033.
- [12] Z. He, M. Li, Y. Li, J. Zhu, Y. Jiang, W. Meng, H. Zhou, L. Wang, L. Dai, Flexible electrospun carbon nanofiber embedded with TiO2 as excellent negative electrode for vanadium redox flow battery, Electrochim. Acta. 281 (2018) 601–610. https://doi.org/10.1016/j.electacta.2018.06.011.
- [13] P.C. Ghimire, R. Schweiss, G.G. Scherer, N. Wai, T.M. Lim, A. Bhattarai, T.D. Nguyen, Q. Yan, Titanium carbide-decorated graphite felt as high performance negative electrode in vanadium redox flow batteries, J. Mater. Chem. A. 6 (2018) 6625–6632. https://doi.org/10.1039/c8ta00464a.
- [14] H. Gursu, M. Gencten, Y. Sahin, Preparation of sulphur-doped graphene-based

- electrodes by cyclic voltammetry: A potential application for vanadium redox flow battery, Int. J. Electrochem. Sci. 13 (2018) 875–885. https://doi.org/10.20964/2018.01.71.
- [15] D.M. Kabtamu, A.W. Bayeh, T.C. Chiang, Y.C. Chang, G.Y. Lin, T.H. Wondimu, S.K. Su, C.H. Wang, TiNb 2 O 7 nanoparticle-decorated graphite felt as a high-performance electrode for vanadium redox flow batteries, Appl. Surf. Sci. 462 (2018) 73–80. https://doi.org/10.1016/j.apsusc.2018.08.101.
- [16] J.D. Milshtein, K.M. Tenny, J.L. Barton, J. Drake, R.M. Darling, F.R. Brushett, Quantifying Mass Transfer Rates in Redox Flow Batteries, J. Electrochem. Soc. 164 (2017) E3265–E3275. https://doi.org/10.1149/2.0201711jes.
- [17] J.Q. Chen, B.G. Wang, H.L. Lv, Numerical simulation and experiment on the electrolyte flow distribution for all vanadium redox flow battery, Adv. Mater. Res. 236–238 (2011) 604–607. https://doi.org/10.4028/www.scientific.net/AMR.236-238.604.
- [18] D.S. Aaron, Q. Liu, Z. Tang, G.M. Grim, A.B. Papandrew, A. Turhan, T.A. Zawodzinski, M.M. Mench, Dramatic performance gains in vanadium redox flow batteries through modified cell architecture, J. Power Sources. 206 (2012) 450–453. https://doi.org/10.1016/j.jpowsour.2011.12.026.
- [19] R.M. Darling, M.L. Perry, The Influence of Electrode and Channel Configurations on Flow Battery Performance, J. Electrochem. Soc. 161 (2014) A1381–A1387. https://doi.org/10.1149/2.0941409jes.
- [20] X. Ke, J.M. Prahl, I.J.D. Alexander, J.S. Wainright, T.A. Zawodzinski, R.F. Savinell, Rechargeable redox flow batteries: Flow fields, stacks and design considerations, Chem. Soc. Rev. 47 (2018) 8721–8743. https://doi.org/10.1039/c8cs00072g.
- [21] D. Schmal, J. Van Erkel, P.J. Van Duin, Mass transfer at carbon fibre electrodes, J. Appl. Electrochem. 16 (1986) 422–430. https://doi.org/10.1007/BF01008853.
- [22] A.A. Shah, M.J. Watt-Smith, F.C. Walsh, A dynamic performance model for redox-flow batteries involving soluble species, Electrochim. Acta. 53 (2008) 8087–8100. https://doi.org/10.1016/j.electacta.2008.05.067.
- [23] X. You, Q. Ye, P. Cheng, The Dependence of Mass Transfer Coefficient on the Electrolyte Velocity in Carbon Felt Electrodes: Determination and Validation, J. Electrochem. Soc. 164 (2017) E3386–E3394. https://doi.org/10.1149/2.0401711jes.
- [24] V.P. Nemani, K.C. Smith, Assignment of Energy Loss Contributions in Redox Flow Batteries using Exergy Destruction Analysis, J. Power Sources. 447 (2020) 227371. https://doi.org/10.1016/j.jpowsour.2019.227371.
- [25] J.S. Newman, K. Thomas-Alyea, Electrochemical Systems, 3rd ed., Prentice Hall, Englewood Cliffs, N.J. 2004.
- [26] J. Leadbetter, L.G. Swan, Selection of battery technology to support grid-integrated renewable electricity, J. Power Sources. 216 (2012) 376–386. https://doi.org/10.1016/j.jpowsour.2012.05.081.
- [27] J. Leadbetter, L. Swan, Battery storage system for residential electricity peak demand shaving, Energy Build. 55 (2012) 685–692. https://doi.org/10.1016/j.enbuild.2012.09.035.
- [28] E. Sum, M. Rychcik, M. Skyllas-kazacos, Investigation of the V(V)/V(IV) system for use in the positive half-cell of a redox battery, J. Power Sources. 16 (1985) 85–95.

- https://doi.org/10.1016/0378-7753(85)80082-3.
- [29] S. Zhong, M. Skyllas-Kazacos, Electrochemical behaviour of vanadium(V)/vanadium(IV) redox couple at graphite electrodes, J. Power Sources. 39 (1992) 1–9. https://doi.org/10.1016/0378-7753(92)85001-Q.
- [30] X.G. Li, K.L. Huang, S.Q. Liu, L.Q. Chen, Electrochemical behavior of diverse vanadium ions at modified graphite felt electrode in sulphuric solution, J. Cent. South Univ. Technol. (English Ed. 14 (2007) 51–56. https://doi.org/10.1007/s11771-007-0011-6.
- [31] T. Yamamura, N. Watanabe, T. Yano, Y. Shiokawa, Electron-transfer kinetics of Np3+/Np4+, NpO 2+/NpO22+, V2+/V 3+, and VO2+/VO2+ at carbon electrodes, J. Electrochem. Soc. 152 (2005) A830–A836. https://doi.org/10.1149/1.1870794.
- [32] J. González-García, P. Bonete, E. Expósito, V. Montiel, A. Aldaz, R. Torregrosa-Maciá, Characterization of a carbon felt electrode: Structural and physical properties, J. Mater. Chem. 9 (1999) 419–426. https://doi.org/10.1039/a805823g.
- [33] K. Kato, K. Kano, T. Ikeda, Electrochemical Characterization of Carbon Felt Electrodes for Bulk Electrolysis and for Biocatalyst-Assisted Electrolysis, J. Electrochem. Soc. 147 (2000) 1449–1453. https://doi.org/10.1149/1.1393376.
- [34] Q. Xu, L. Qin, H. Su, L. Xu, P. Leung, C. Yang, H. Li, Electrochemical and Transport Characteristics of V(II)/V(III) Redox Couple in a Nonaqueous Deep Eutectic Solvent: Temperature Effect, J. Energy Eng. 143 (2017) 04017051. https://doi.org/10.1061/(ASCE)EY.1943-7897.0000484.
- [35] G. Qiu, A.S. Joshi, C.R. Dennison, K.W. Knehr, E.C. Kumbur, Y. Sun, 3-D pore-scale resolved model for coupled species/charge/fluid transport in a vanadium redox flow battery, Electrochim. Acta. 64 (2012) 46–64. https://doi.org/10.1016/j.electacta.2011.12.065.
- [36] M.D.R. Kok, R. Jervis, T.G. Tranter, M.A. Sadeghi, D.J.L. Brett, P.R. Shearing, J.T. Gostick, Mass transfer in fibrous media with varying anisotropy for flow battery electrodes: Direct numerical simulations with 3D X-ray computed tomography, Chem. Eng. Sci. 196 (2019) 104–115. https://doi.org/10.1016/j.ces.2018.10.049.
- [37] T. Tichter, D. Andrae, J. Mayer, J. Schneider, M. Gebhard, C. Roth, Theory of cyclic voltammetry in random arrays of cylindrical microelectrodes applied to carbon felt electrodes for vanadium redox flow batteries, Phys. Chem. Chem. Phys. 21 (2019) 9061–9068. https://doi.org/10.1039/c9cp00548j.
- [38] M.A. Hamid, K.C. Smith, Modeling the Transient Effects of Pore-Scale Convection and Redox Reactions in the Pseudo-Steady Limit, J. Electrochem. Soc. 167 (2020) 013521. https://doi.org/10.1149/2.0212001jes.
- [39] X. Hu, S. Stanton, L. Cai, R.E. White, Model order reduction for solid-phase diffusion in physics-based lithium ion cell models, J. Power Sources. 218 (2012) 212–220. https://doi.org/10.1016/j.jpowsour.2012.07.007.
- [40] J. Huang, Diffusion impedance of electroactive materials, electrolytic solutions and porous electrodes: Warburg impedance and beyond, Electrochim. Acta. 281 (2018) 170–188. https://doi.org/10.1016/j.electacta.2018.05.136.
- [41] T. Jacobsen, K. West, Diffusion impedance in planar, cylindrical and spherical symmetry, Electrochim. Acta. 40 (1995) 255–262. https://doi.org/10.1016/0013-4686(94)E0192-3.
- [42] J. Bisquert, G. Garcia-Belmonte, F. Fabregat-Santiago, P.R. Bueno, Theoretical

- models for ac impedance of finite diffusion layers exhibiting low frequency dispersion, J. Electroanal. Chem. 499 (1999) 112–120. https://doi.org/10.1016/S0022-0728(99)00346-0.
- [43] K.C. Smith, R.D. Dmello, Na-Ion Desalination (NID) Enabled by Na-Blocking Membranes and Symmetric Na-Intercalation: Porous-Electrode Modeling, J. Electrochem. Soc. 163 (2016) A530–A539. https://doi.org/10.1149/2.0761603jes.
- [44] K.C. Smith, Theoretical evaluation of electrochemical cell architectures using cation intercalation electrodes for desalination, Electrochim. Acta. 230 (2017) 333–341. https://doi.org/10.1016/j.electacta.2017.02.006.
- [45] S. Liu, K.C. Smith, Quantifying the Trade-offs between Energy Consumption and Salt Removal Rate in Membrane-free Cation Intercalation Desalination, Electrochim. Acta. 271 (2018) 652–665. https://doi.org/10.1016/j.electacta.2018.03.065.
- [46] D.L. Parkhurst, C.A.J. Appelo, User's guide to PHREEQC (Version 2): A computer program for speciation, batch-reaction, one-dimensional transport, and inverse geochemical calculations, Denver, CO, 1999.
- [47] K.C. Smith, Y.-M. Chiang, W. Craig Carter, Maximizing Energetic Efficiency in Flow Batteries Utilizing Non-Newtonian Fluids, J. Electrochem. Soc. 161 (2014) A486–A496. https://doi.org/10.1149/2.011404jes.
- [48] F.Y. Fan, W.H. Woodford, Z. Li, N. Baram, K.C. Smith, A. Helal, G.H. McKinley, W.C. Carter, Y.-M. Chiang, Polysulfide Flow Batteries Enabled by Percolating Nanoscale Conductor Networks, Nano Lett. 14 (2014) 2210–2218. https://doi.org/10.1021/nl500740t.
- [49] T. Wei, F.Y. Fan, A. Helal, K.C. Smith, G.H. Mckinley, Y.-M. Chiang, J.A. Lewis, Biphasic Electrode Suspensions for Li-Ion Semi-Solid Flow Cells with High Energy Density, Fast Charge Transport, and Low-Dissipation Flow, Adv. Energy Mater. (2015) 1500535. https://doi.org/10.1002/aenm.201500535.
- [50] Z. Li, K.C. Smith, Y. Dong, N. Baram, F.Y. Fan, J. Xie, P. Limthongkul, W.C. Carter, Y.M. Chiang, Aqueous semi-solid flow cell: Demonstration and analysis, Phys. Chem. Chem. Phys. 15 (2013) 15833–15839. https://doi.org/10.1039/c3cp53428f.
- [51] D.A. Edwards, M. Shapiro, H. Brenner, Dispersion and reaction in two-dimensional model porous media, Phys. Fluids A Fluid Dyn. 5 (1993) 837–848. https://doi.org/10.1063/1.858631.
- [52] B.B. Dykaar, P.K. Kitanidis, Macrotransport of a biologically reacting solute through porous media, Water Resour. Res. 32 (1996) 307–320. https://doi.org/10.1029/95WR03241.
- [53] H. Brenner, Dispersion Resulting from Flow through Spatially Periodic Porous Media, Philos. Trans. R. Soc. A Math. Phys. Eng. Sci. 297 (1980) 81–133. https://doi.org/10.1098/rsta.1980.0205.
- [54] H. Brenner, P.M. Adler, Dispersion Resulting from Flow through Spatially Periodic Porous Media II. Surface and Intraparticle Transport, Philos. Trans. R. Soc. A Math. Phys. Eng. Sci. 307 (1982) 149–200. https://doi.org/10.1098/rsta.1982.0108.
- [55] D.A. Edwards, M. Shapiro, H. Brenner, Dispersion and reaction in two-dimensional model porous media, Phys. Fluids A Fluid Dyn. 5 (1993) 837. https://doi.org/10.1063/1.858631.
- [56] W.G. Gray, A derivation of the equations for multi-phase transport, Chem. Eng. Sci.

- 30 (1975) 229–233. https://doi.org/https://doi.org/10.1016/0009-2509(75)80010-8.
- [57] S. Whitaker, The transport equations for multi-phase systems, Chem. Eng. Sci. 28 (1973) 139–147.
- [58] J. Newman, W. Tiedemann, Porous-electrode theory with battery applications, AIChE J. 21 (1975) 25–41. https://doi.org/10.1002/aic.690210103.
- [59] J. Luo, A. Sam, B. Hu, C. DeBruler, X. Wei, W. Wang, T.L. Liu, Unraveling pH dependent cycling stability of ferricyanide/ferrocyanide in redox flow batteries, Nano Energy. 42 (2017) 215–221. https://doi.org/10.1016/J.NANOEN.2017.10.057.
- [60] K. Gong, F. Xu, J.B. Grunewald, X. Ma, Y. Zhao, S. Gu, Y. Yan, All-Soluble All-Iron Aqueous Redox-Flow Battery, ACS Energy Lett. 1 (2016) 89–93. https://doi.org/10.1021/acsenergylett.6b00049.
- [61] N.G. Tsierkezos, A. Knauer, U. Ritter, Thermodynamic investigation of ferrocyanide/ferricyanide redox system on nitrogen-doped multi-walled carbon nanotubes decorated with gold nanoparticles, Thermochim. Acta. 576 (2014) 1–8. https://doi.org/10.1016/J.TCA.2013.11.020.
- [62] P. Kulesza, T. Jedral, Z. Galus, The electrode kinetics of the Fe(CN)63-/Fe(CN)64- system on the platinum rotating electrode in the presence of different anions, J. Electroanal. Chem. Interfacial Electrochem. 109 (1980) 141– 149.
- [63] V. V. Nikonenko, N.D. Pismenskaya, E.I. Belova, P. Sistat, P. Huguet, G. Pourcelly, C. Larchet, Overlimiting Current and Shock Electrodialysis in Porous Media, Adv. Colloid Interface Sci. 160 (2010) 101–123.
- [64] V. V. Nikonenko, N.D. Pismenskaya, E.I. Belova, P. Sistat, P. Huguet, G. Pourcelly, C. Larchet, Intensive current transfer in membrane systems: Modelling, mechanisms and application in electrodialysis, Adv. Colloid Interface Sci. 160 (2010) 101–123. https://doi.org/10.1016/J.CIS.2010.08.001.
- [65] D. Deng, E.V. Dydek, J.-H. Han, S. Schlumpberger, A. Mani, B.Z.M.Z. Bazant, Overlimiting Current and Shock Electrodialysis in Porous Media, Langmuir. 29 (2013) 16167–16177.
- [66] P. Grathwohl, D. Lerner, Natural attenuation of organic pollutants in groundwater, J. Contam. Hydrol. 53 (2001) 173–174. https://doi.org/10.1016/s0169-7722(01)00165-6.
- [67] G. Yossifon, H.-C. Chang, Selection of Nonequilibrium Overlimiting Currents: Universal Depletion Layer Formation Dynamics and Vortex Instability, Phys. Rev. Lett. 101 (2008) 254501.
- [68] Y. Jaluria, K. Torrance, Computational heat transfer, Hemisphere Publishing Corporation, 1986.
- [69] V.P. Nemani, K.C. Smith, Uncovering the role of flow rate in redox-active polymer flow batteries: simulation of reaction distributions with simultaneous mixing in tanks, Electrochem. Acta. 247 (2017) 475–485. https://doi.org/10.1016/j.electacta.2017.07.008.
- [70] X. Hu, S. Stanton, L. Cai, R.E. White, A linear time-invariant model for solid-phase diffusion in physics-based lithium ion cell models, J. Power Sources. 214 (2012) 40–50. https://doi.org/10.1016/j.jpowsour.2012.04.040.
- [71] B. Gustavsen, A. Semlyen, Rational approximation of frequency domain responses

- by vector fitting, IEEE Trans. Power Deliv. 14 (1999) 1052–1059. https://doi.org/10.1109/61.772353.
- [72] B. Gustavsen, Improving the pole relocating properties of vector fitting, IEEE Trans. Power Deliv. 21 (2006) 1587–1592. https://doi.org/10.1109/TPWRD.2005.860281.
- [73] D. Deschrijver, M. Mrozowski, T. Dhaene, D. De Zutter, Macromodeling of multiport systems using a fast implementation of the vector fitting method, IEEE Microw. Wirel. Components Lett. 18 (2008) 383–385. https://doi.org/10.1109/LMWC.2008.922585.
- [74] J.P. Sørensen, W.E. Stewart, Computation of forced convection in slow flow through ducts and packed beds-III. Heat and mass transfer in a simple cubic array of spheres, Chem. Eng. Sci. 29 (1974) 827–832. https://doi.org/10.1016/0009-2509(74)80201-0.
- [75] P.W. Appel, J. Newman, Application of the limiting current method to mass transfer in packed beds at very low reynolds numbers, AIChE J. 22 (1976) 979–984. https://doi.org/10.1002/aic.690220605.
- [76] P.S. Fedkiw, J. Newman, Mass-transfer coefficients in packed beds at very low reynolds numbers, Int. J. Heat Mass Transf. 25 (1982) 935–943. https://doi.org/10.1016/0017-9310(82)90069-2.
- [77] A. Caprani, C. Deslouis, S. Robin, B. Tribollet, Transient mass transfer at partially blocked electrodes: a way to characterize topography, J. Electroanal. Chem. 238 (1987) 67–91. https://doi.org/10.1016/0022-0728(87)85166-5.

Supplementary Information for

A Bottom-Up, Multi-Scale Theory for Transient Mass Transport of Redox-Active Species through Porous Electrodes beyond the Pseudo-Steady Limit

Md Abdul Hamida and Kyle C. Smitha,b,c,d,*

^a Department of Mechanical Science and Engineering,
 University of Illinois at Urbana-Champaign, Urbana, IL 61801, USA
 ^b Department of Materials Science and Engineering,
 University of Illinois at Urbana-Champaign, Urbana, IL 61801, USA
 ^c Computational Science and Engineering Program,
 University of Illinois at Urbana-Champaign, Urbana, IL 61801, USA
 ^d Beckman Institute for Advanced Science and Technology,
 University of Illinois at Urbana-Champaign, Urbana, IL 61801, USA

*Corresponding author: kcsmith@illinois.edu

A. Derivation of the criteria for the validity of uniform surface-concentration boundary conditions.

Here we derive the criteria that must be satisfied to use a uniform surface concentration boundary condition for active soluble species undergoing a coupled heterogenous redox $(s_R R^{z_R} + s_O O^{z_O} + e^- \rightleftharpoons 0)$, where the electromigration flux contributions of such species are negligible in solution. The transient local concentration of species i is governed by the following mass conservation equation (MCE):

$$\frac{\partial c_i}{\partial t} + \nabla \cdot (\mathbf{j}_i) = 0 \tag{A1}$$

Here $\mathbf{j}_i = -D_i \nabla c_i - \frac{Z_i F}{RT} D_i c_i \nabla \phi + \mathbf{u}^{\bullet} c_i$ is the total flux of species i. Note that i appearing as subscript denotes either species R or O, not to be confused with i appearing as denotation of current density. The flux \mathbf{j}_i is also not to be confused with the imaginary unit $j = \sqrt{-1}$ appearing later. We assume that solid/solution interfaces are stationary and impenetrable to bulk flow, resulting in $\mathbf{u}^{\bullet} \cdot \mathbf{n}|_s = 0$. The coupled production and consumption of species is enforced by the boundary condition (BC) as $\mathbf{j}_R \cdot \hat{\mathbf{n}}|_s = -\mathbf{j}_O \cdot \hat{\mathbf{n}}|_s$ or $D_R \frac{\partial c_R}{\partial n}|_s = -D_O \frac{\partial c_O}{\partial n}|_s$, since electromigration is assumed to be negligible and because electrode surfaces are impermeable to solution. The current density i at the solid/solution interface is coupled to the flux of either species as a result of redox reaction stoichiometry:

$$i = \frac{F}{s_i} \langle j_i \rangle_s = -\frac{F}{s_i} D_i \frac{\partial c_i}{\partial n} \Big|_s = f(\eta)$$
(A2)

Here, overpotential is expressed as $\eta = \phi_s(t) - \phi_e(t) - \phi_{eq}(c_{O,s}, c_{R,s})$, and we assume that the oxidation reaction produces a positive current, while reduction produces a negative current. Redox reaction kinetics relate i to overpotential η . Using Taylor series expansion with respect to a certain current density i^* that corresponds to a certain

overpotential $\eta^* = \phi_s(t) - \phi_e(t) - \phi_{eq}(c_{O,s}^*, c_{R,s}^*)$, we obtain a linear expansion of current density that will later be used to derive validity conditions on the basis of scaling analysis:

$$i \approx i^* + \frac{\partial i}{\partial \phi_s}\Big|_* \left(\phi_s - \phi_s^*\right) + \frac{\partial i}{\partial \phi_e}\Big|_* \left(\phi_e - \phi_e^*\right) + \frac{\partial i}{\partial c_{R,S}}\Big|_* \left(c_{R,S} - c_{R,S}^*\right) + \frac{\partial i}{\partial c_{O,S}}\Big|_* \left(c_{O,S} - c_{O,S}^*\right)$$

or,
$$i \approx i^* + \frac{\partial i}{\partial \eta^0}\Big|_* \left(\Delta \phi|_S - \Delta \phi|_S^*\right) + \frac{\partial i}{\partial c_{R,S}}\Big|_* \left(c_{R,S} - c_{R,S}^*\right) + \frac{\partial i}{\partial c_{O,S}}\Big|_* \left(c_{O,S} - c_{O,S}^*\right)$$
 (A3)

Here, $\Delta \phi|_s = \phi_s - \phi_e$ is a driving potential difference between the solid and the electrolyte, and $\eta^0 = \phi_s - \phi_e - \phi_{eq}^0$ is the overpotential at standard conditions. Using the law of mass action with rate constants for oxidation k_{ox} and reduction k_{red} we find:

$$i = f(\eta) = F(k_f c_{R,s} - k_b c_{O,s}) = F(k_{ox} c_{R,s} - k_{red} c_{O,s})$$
(A4)

Using this kinetics formalism, the relevant partial derivatives of current density i are:

$$\frac{\partial i}{\partial \eta^0} = F\left(c_{R,s} \frac{\partial k_{ox}}{\partial \eta^0} - c_{O,s} \frac{\partial k_{red}}{\partial \eta^0}\right) \tag{A5a}$$

$$\frac{\partial i}{\partial c_{O,S}} = F\left(c_{R,S} \frac{\partial k_{ox}}{\partial \eta^0} \frac{\partial \eta^0}{\partial c_{O,S}} - c_{O,S} \frac{\partial k_{red}}{\partial \eta^0} \frac{\partial \eta^0}{\partial c_{O,S}} - k_{red}\right) \tag{A5b}$$

$$\frac{\partial i}{\partial c_{R,S}} = F\left(k_{ox} + c_{R,S} \frac{\partial k_{ox}}{\partial \eta^0} \frac{\partial \eta^0}{\partial c_{R,S}} - c_{O,S} \frac{\partial k_{red}}{\partial \eta^0} \frac{\partial \eta^0}{\partial c_{R,S}}\right) \tag{A5c}$$

Using Butler-Volmer kinetics with $k_{ox} = k^0 exp[(1-\alpha)F \,\eta^0/RT]$ and $k_{red} = k^0 exp[-\alpha F \,\eta^0/RT]$, these derivatives are $\partial i/\partial \eta^0 = F^2/RT \, \left[(1-\alpha)k_{ox}c_{R,s} + \alpha \, k_{red}c_{O,s} \right]$, $\partial i/\partial c_{R,s} = Fk_{ox}$ and $\partial i/\partial c_{O,s} = -Fk_{red}$. Using Eqs. A2 and A3, we obtain a linear, Robintype BC that couples the concentration of both species to the gradient of their concentrations at the solid/solution interface (Eq. A6).

After rearrangement Eq. A6 reduces to the following expression:

$$\frac{D_{i}}{s_{i}} \frac{\partial c_{i}}{\partial n} \Big|_{s} + k_{ox}^{*} c_{R,s} - k_{red}^{*} c_{O,s} = -\frac{i^{*}}{F} - k_{ox}^{*} c_{R,s}^{*} \left[\frac{F}{RT} (\Delta \phi |_{s} - \Delta \phi |_{s}^{*}) \right] + \left(k_{ox}^{*} c_{R,s}^{*} - k_{red}^{*} c_{O,s}^{*} \right) \left[1 + \alpha \frac{F}{RT} (\Delta \phi |_{s} - \Delta \phi |_{s}^{*}) \right]$$
(A6)

Nondimensionalization of the terms in Eq. A6 enables us to perform scaling analysis. To do so we choose a nondimensional normal coordinate $\tilde{n}=n/b$ with characteristic pore dimension b, a nondimensional surface concentration $\tilde{c}_i|_s=(c_i/c_i^*)|_s$, and a nondimensional potential difference $\Delta \tilde{\phi}=\Delta \phi F/(RT)$:

$$\frac{1}{s_{i}} \left(\frac{\partial \tilde{c}_{i}}{\partial \tilde{n}} \Big|_{s} \right) + \frac{k_{ox}^{*} b}{D_{i}} \left[\frac{c_{R,s}^{*}}{c_{i,s}^{*}} \right] \left(\tilde{c}_{R,s} \right) - \frac{k_{red}^{*} b}{D_{i}} \left[\frac{c_{O,s}^{*}}{c_{i,s}^{*}} \right] \left(\tilde{c}_{O,s} \right) = -\frac{b i^{*}}{F D_{i} c_{i,s}^{*}} + \frac{k_{ox}^{*} b}{D_{i}} \left[\frac{c_{R,s}^{*}}{c_{i,s}^{*}} \right] \left[1 - (1 - \alpha) \left(\Delta \tilde{\phi} \Big|_{s} - \tilde{\phi} \Big|_{s}^{*} \right) \right] - \frac{k_{red}^{*} b}{D_{i}} \left[\frac{c_{O,s}^{*}}{c_{i,s}^{*}} \right] \left[1 + \alpha \left(\Delta \tilde{\phi} \Big|_{s} - \Delta \tilde{\phi} \Big|_{s}^{*} \right) \right] \tag{A7}$$

To approach a Dirichlet condition, thus representing a boundary condition that depends solely on the concentration of either species but not on its gradient, requires that the gradient term in Eq. A7 (i.e., $\partial \tilde{c}_i/\partial \tilde{n}|_s$) vanish relative to the concentration-dependent term. We now consider characteristic scales for the concentration of each species $(c_{O,s} \sim c_{O,s}^*$ and $c_{R,s} \sim c_{R,s}^*$) and for length $(n \sim b)$, which require that $(\partial \tilde{c}_i/\partial \tilde{n})|_s \sim 1$, $\tilde{c}_{R,s} \sim 1$, and $\tilde{c}_{O,s} \sim 1$). On this basis we argue that the gradient term in Eq. A7 vanishes relative to the concentration-dependent terms when either of the two criteria are satisfied:

$$1 \ll \left| \frac{k_{red}^* b}{D_i} \frac{c_{O,S}^*}{c_{is}^*} \right| \qquad \text{or} \qquad 1 \ll \left| \frac{k_{OX}^* b}{D_i} \frac{c_{R,S}^*}{c_{is}^*} \right| \tag{A8}$$

For oxidized and reduced species these conditions can be written as,

For
$$0: 1 \ll \left| \frac{k_{red}^* b}{D_O} \right|$$
; or $1 \ll \left| \frac{k_{red}^* b}{D_O} \left(\frac{k_{ox}^*}{k_{red}^*} \frac{c_{R,S}^*}{c_{O,S}^*} \right) \right|$ (A9a)

For
$$R: 1 \ll \left| \frac{k_{ox}^* b}{D_R} \left(\frac{k_{red}^* c_{o,s}^*}{k_{ox}^*} \frac{c_{o,s}^*}{c_{R,s}^*} \right) \right|;$$
 or $1 \ll \left| \frac{k_{ox}^* b}{D_R} \right|$ (A9b)

The terms inside the parentheses in Eq. A9 can be simplified by utilizing the de Donder relation $(k_{ox}^*/k_{red}^* = exp(F\eta^0/RT))$ and a logarithm identity $(c_{o,s}^*/c_{R,s}^* = exp[ln(c_{o,s}^*/c_{R,s}^*)])$, by which we obtain $(k_{ox}^*c_{R,s}^*)/(k_{red}^*c_{o,s}^*) = exp[F/RT(\eta^0 - ln(c_o^*/c_R^*)|_s)] = exp(F\eta^*/RT)$. Introducing the definition of a Damköhler number for both reduction and oxidation as $Da_{red} = k_{red} \ b/D_o$ and $Da_{ox} = k_{ox} \ b/D_R$, the required criteria to approach a uniform surface condition are given as:

$$Da_{red} \gg \min[1, exp(-F\eta^*/RT)]$$
 and $Da_{ox} \gg \min[1, exp(F\eta^*/RT)]$ (A10)

Thus, the respective Damköhler numbers must be sufficiently large to assure that the uniform surface concentration boundary is valid.

B. Validity criterion for periodic boundary conditions

Here we revisit the validity criteria for imposing periodic boundary conditions for periodic microstructures – an assumption invoked *ad hoc* in section 2.1 – by performing scaling analysis of electrolyte flow through an electrode, similar to our approach used in the pseudo-steady limit (Ref. [1]) with the exceptions that (1) we consider a non-recirculating cell configuration and (2) we perform our scaling analysis in the frequency domain with the aid of the transfer functions introduced already. Following our previous work, we analyze the time-dependent average concentration $\langle c \rangle_r$ within the electrode/reactor using an integral MCE assuming an electrolyte feed with certain uniform concentration of redox-active species flowing in c^{in} with a volumetric flow rate \dot{V} :

$$\frac{d(\varepsilon A_c L_r \langle c \rangle_r)}{dt} = \dot{V} c^{in} - A_c |\boldsymbol{u}_s| [\langle c \rangle_r - \mathcal{F}^{-1} \{\langle N \rangle_{\parallel} (\bar{c}_s - \langle \bar{c} \rangle_r)\}] + \frac{a L_r A_c D}{b} \mathcal{F}^{-1} \big\{ \langle \widetilde{Sh} \rangle (\bar{c}_s - \langle \bar{c} \rangle_r) \big\} \ \ (\text{B1})$$

Here, the rightmost two terms, which contain the transfer functions $\langle N \rangle_{\parallel}$ and $\langle \widetilde{Sh} \rangle$, are respectively a result of the rate of solute advection through the outlet and the rate of solute

production by virtue of electrochemical reactions at the solid/solution interface. A_c and L_r are respectively the electrode's cross sectional area normal to the superficial velocity u_s and the electrode's length in the streamwise direction. a is the electrode's surface area per unit volume. Fourier transformation of this equation simplifies this expression to:

$$j\omega\varepsilon A_c L_r \langle \bar{c} \rangle_r = \dot{V}\bar{c}^{in} - A_c |\mathbf{u}_s| [\langle \bar{c} \rangle_r - \langle N \rangle_{\parallel} (\bar{c}_s - \langle \bar{c} \rangle_r)] + \frac{aL_r A_c D}{h} \langle \widetilde{Sh} \rangle (\bar{c}_s - \langle \bar{c} \rangle_r)$$
(B2)

Similar to our previous work [1], we require the ratio of characteristic streamwise $(\Delta c)^m_{\parallel}$ and transverse $(\Delta c)^m_{\perp}$ concentration differences to be sufficiently small at the macroscopic scale in order to assure that streamwise concentration differences are sufficiently small, ultimately requiring that the following nondimensional quotient $\Delta \hat{c}$ satisfy $\Delta \hat{c} \ll 1$:

$$\Delta \hat{c} = \frac{b}{L_r} \cdot \left| \frac{\langle \bar{c} \rangle_r - \bar{c}^{in}}{\langle \bar{c} \rangle_r - \bar{c}_s} \right| \sim \left| \frac{(\Delta c)_{i,\parallel}^m}{(\Delta c)_{i,\parallel}^m} \right|$$
(B3)

By solving the Fourier-transformed MCE for $\langle \bar{c} \rangle_r - \bar{c}^{in}$ we obtain the following criterion after significant simplification to assure the validity of periodic boundary conditions:

$$\Delta \hat{c} = \frac{1}{Pe} \left| \frac{2\pi j f^* \varepsilon \langle \mathbb{C} \rangle}{1 - \langle \mathbb{C} \rangle} - ab \langle \widetilde{Sh} \rangle - \frac{b}{L_r} Pe \langle N \rangle_{\parallel} \right| \ll 1$$
 (B4)

Hence, the validity of using periodic boundary conditions is, in a sense, a recursive criterion because it depends not only on input nondimensional parameters (Pe, f^*, ab , and b/L_r) but also on the nondimensional transfer functions $\langle N \rangle_{\parallel}$ and $\langle \widetilde{Sh} \rangle$ that are outputs produced based on those input parameters. In practice, $\langle N \rangle_{\parallel}$ and $\langle \widetilde{Sh} \rangle$ would first be predicted and $\Delta \hat{c}$ would subsequently be calculated to verify the self-consistency of such simulations performed using periodic boundary conditions. Further, Eq. B4 is a criterion that is *frequency- or mode-specific*, and, hence, it is advisable to evaluate $\Delta \hat{c}$ at frequencies that are *representative* of the total response.

C. Equivalence of spectral Sherwood number $\langle \widetilde{Sh} \rangle$ at vanishing frequency with Sherwood number $\langle Sh \rangle$ in the pseudo-steady limit

Here we demonstrate the equivalence between the spectral Sherwood number $\langle \widetilde{Sh} \rangle$ in the limit of $\omega \to 0$ with the conventional Sherwood number obtained in the pseudosteady limit. For the pseudo-steady limit, we consider the auxiliary problem that we introduced previously in Ref. [1]. The auxiliary problem is described by a steady MCE in terms of the time-independent contribution $c_h(\mathbf{r})$ to the time- and space- dependent concentration field $c(t,\mathbf{r})$ as:

$$\nabla \cdot (\boldsymbol{u}^{\bullet} c_h - D \nabla c_h) = -\sigma; \qquad c_h|_{s} = 0 \tag{C1}$$

where $c_h(r) = c(r,t) - c_s(t)$ and the source term σ represents the temporal rate of change in surface concentration $\sigma = \partial c_s/\partial t$. The conventional Sherwood number is defined in terms of $c_h(r)$ using the film law of mass transport. In the present study, the unsteady conjugate problem is replaced by a Fourier-transformed MCE (Eq. 4) where the

spectral Sherwood number $\langle \widetilde{Sh} \rangle$ is defined by Eq. 6 from the main text. To demonstrate the equivalence of the Fourier transformed MCE (Eq. 4) with the auxiliary problem's MCE (Eq. B1), we define $\delta = (\bar{c} - \bar{c}_s)/\bar{c}_s$, and we substitute it back into Eq. 4 from the main text to produce the following:

$$\frac{1}{i\omega}\nabla\cdot(\boldsymbol{u}^{\bullet}\delta-D\nabla\delta)=-(1+\delta);\qquad \delta|_{s}=0$$
(C2)

Scaling analysis of Eq. C2 with a characteristic length scale b and a characteristic velocity U reveals that its righthand side approaches unity for vanishing frequency (i.e., $\lim_{\omega \to 0} (1 + \delta) = 1$), based either on characteristic scales for advection $(\delta \sim \omega b/U)$ or for diffusion ($\delta \sim \omega b^2/D_i$). In this limit Eq. C2 approaches the following form:

$$\nabla \cdot (\boldsymbol{u}^{\bullet} \delta - D \nabla \delta) = -j \omega; \qquad \delta|_{s} = 0 \tag{C3}$$

Since δ is a complex number, we expand it in terms of real and imaginary parts $\delta = \delta_{Re} + j \, \delta_{Im}$ to obtain a single PDE for the real part $(\nabla \cdot (\boldsymbol{u}^{\blacksquare} \delta_{Re} - D \nabla \delta_{Re}) = 0$ with $\delta_{Re}|_{s} = 0)$ and a single PDE for the imaginary part $(\nabla \cdot (\boldsymbol{u}^{\blacksquare} \delta_{Im} - D \nabla \delta_{Im}) = -\omega$ with $\delta_{Im}|_{s} = 0)$. The only solution possible for the real component is the trivial solution, i.e., $\delta_{Re} = 0$. Thus, we deduce that $\delta = j \delta_{Im}$, and we solve only for the imaginary component:

$$\nabla \cdot (\boldsymbol{u}^{\bullet} \delta_{Im} - D \nabla \delta_{Im}) = -\omega; \qquad \delta_{Im}|_{s} = 0$$
 (C4)

To verify the equivalence of Eq. C1 and Eq. C4, we define $\delta'_{lm} = \delta_{lm}/\omega$ and $c'_h = c_h/\sigma$ and substitute into the respective equations to obtain:

$$\nabla \cdot (\boldsymbol{u}^{\bullet} \delta'_{lm} - D \nabla \delta'_{lm}) = -1; \qquad \delta'_{lm}|_{s} = 0$$

$$\nabla \cdot (\boldsymbol{u}^{\bullet} c_h' - D \nabla c_h') = -1; \qquad c_h'|_{s} = 0$$

Inspection reveals that solutions to these PDEs are identical, such that $\delta'_{lm}=c'_h$ and $\frac{\delta_{lm}}{\omega}=\frac{c_h}{\sigma}$ are satisfied exactly. By recognizing that surface fluxes are only due to diffusion (and not advection), the associated flux and concentration difference can be expressed in terms of δ as $\langle \bar{j} \rangle_s = -D\langle \partial \bar{c}/\partial n \rangle = -D\langle \partial \delta_{lm}/\partial n \rangle \bar{c}_s$ and $\bar{c}_s - \langle \bar{c} \rangle = -\langle \delta_{lm} \rangle \bar{c}_s$. Therefore, $\langle \widetilde{Sh} \rangle$ approaches the following expression in the limit of vanishing frequency:

$$\lim_{\omega \to 0} \langle \widetilde{Sh} \rangle = \lim_{\omega \to 0} \frac{d}{D} \frac{\langle \overline{j} \rangle_{S}}{\overline{c}_{S} - \langle \overline{c} \rangle} = \frac{d}{\langle \delta_{Im} \rangle} \langle \frac{\partial \delta_{Im}}{\partial n} \rangle = \frac{d}{\frac{\omega}{\sigma} \langle c_{h} \rangle} \frac{\partial c_{h}}{\sigma} \langle \frac{\partial c_{h}}{\partial n} \rangle = \frac{d}{-(c_{S} - \langle c \rangle)} \langle \frac{\partial c}{\partial n} \rangle = \frac{d}{D} \frac{\langle \overline{j}_{S} \rangle}{c_{S} - \langle c \rangle} = \langle Sh \rangle_{PSL}$$
 (C5)

This analysis demonstrates that the value of $\langle \widetilde{Sh} \rangle$ for $\omega \to 0$ must be equal to the value of $\langle Sh \rangle$ obtained in the pseudo-steady limit. This analysis also suggests an alternative interpretation of the transfer function $\langle \widetilde{Sh} \rangle$, i.e., that it is essentially a frequency-dependent version of the Sherwood number. This statement is further supported through comparison between $\lim_{\omega \to 0} \langle \widetilde{Sh} \rangle$ values obtained from present model and $\langle Sh \rangle_{PSL}$ values obtained from pseudo-steady simulations [1], where the percentage deviation observed is found to be within machine precession ($\sim 10^{-15}$ %).

D. Experimentation and model prediction comparison

To compare the predictions of our bottom-up transient model with experimentally obtained polarization values, a redox flow-cell setup was implemented and tested experimentally. To validate the present model with experimental data the flow cell was prepared using a well-prescribed electrode geometry using redox chemistry with well-known electrochemical properties. The reaction chemistry chosen was the ferro/ferricyanide $(Fe(CN)_6^{4-}/Fe(CN)_6^{3-})$ couple dissolved in an aqueous solution along with KCl as supporting salt.

The flow cell consisted of two 200 μm thick graphite foil electrodes (4.5 $cm \times 4.5$ cm) separated by a non-selective polymer separator (NP030 from STERLITECH Corporation). The electrolyte solution was pumped at a rate of 5 mL/min through the triangular channel engraved electrodes (TCEE) to create flow along the length of such channels, as shown in Figs. D2a and D2c. The parallel triangular channels (see Fig. D1a) were engraved using a Trotec laser engraver (Speedy Flexx 400 fiber laser) with 100 μm spacing from valley to valley. A nominal 90 μm deep and 75 μm wide isosceles channel cross-section (Fig. D1d) was determined from the mean values of the Gaussian distribution of measured depth and width for model implementation, as determined from 3D profilometry (Keyence). The nominal channel cross-section area obtained was $3375~\mu m^2$, which coincides with the mean values obtained from Gaussian distribution of measured cross-sectional area for both electrodes (Figs. D1b and D1c). The volume-specific reactive area and total flow area for the electrolyte were calculated from this representative geometry. We note that the channel depth $d_{ch} = 90~\mu m$ was taken as the characteristic length to calculate non-dimensional parameters.

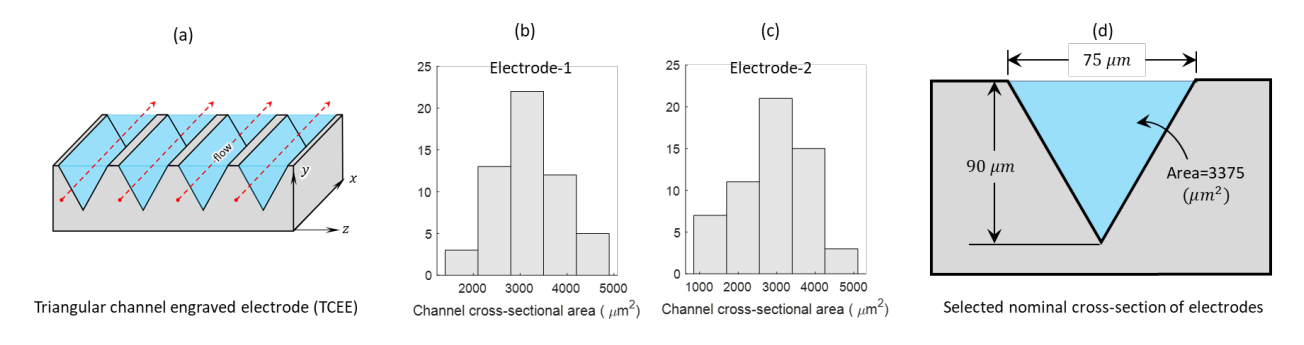


Fig. D1: (a) Schematic of a triangular channel engraved electrode (TCEE) produced by laser engraving of graphite foil. (b, c) Histograms showing Gaussian distribution of the measured cross-sectional area at different locations. Representative channel cross-section approximated for pore-scale model implementation that produces a cross-sectional area close to the average values of the distributions observed in Figs. D1b and D1c.

The electrolyte solution was prepared by dissolving potassium hexacyanoferrate(II) trihydrate, $K_4Fe(CN)_6 \cdot 3H_2O$, and potassium hexacyanoferrate(III), $K_3Fe(CN)_6$, in deionized water. All the chemicals were from Sigma-Aldrich and were used

as received to prepare $350\,mL$ of $15\,mM$ (individual species) solution. High salt concentration ($3\,M\,KCl$) was used to increase the ionic conductivity of the electrolyte as well as to decrease the electromigration of active species. For simplicity, the anodic and cathodic kinetic processes were modeled as symmetric with equal Butler-Volmer transfer coefficients ($\alpha=0.5$) with an identical diffusivity of $D=7\times 10^{-6}\,cm^2/s$ and a rate constant of $k_s=0.1\,cm/s$. The values of D and L_s were taken from published literature [2–7]. From these values the calculated limiting current density L_{lim} , Peclet number L_s 0 pamköhler number L_s 1, and nondimensional flow rate L_s 2 are listed in Table D1. To obtain the transient response of the flow cell, applied current was varied as a square wave as shown in Fig. D2b. During all experiments, each tank was prepared with L_s 2 of electrolyte to ensure that the change in state-of-charge during any charging/discharging step was less than 0.1%.

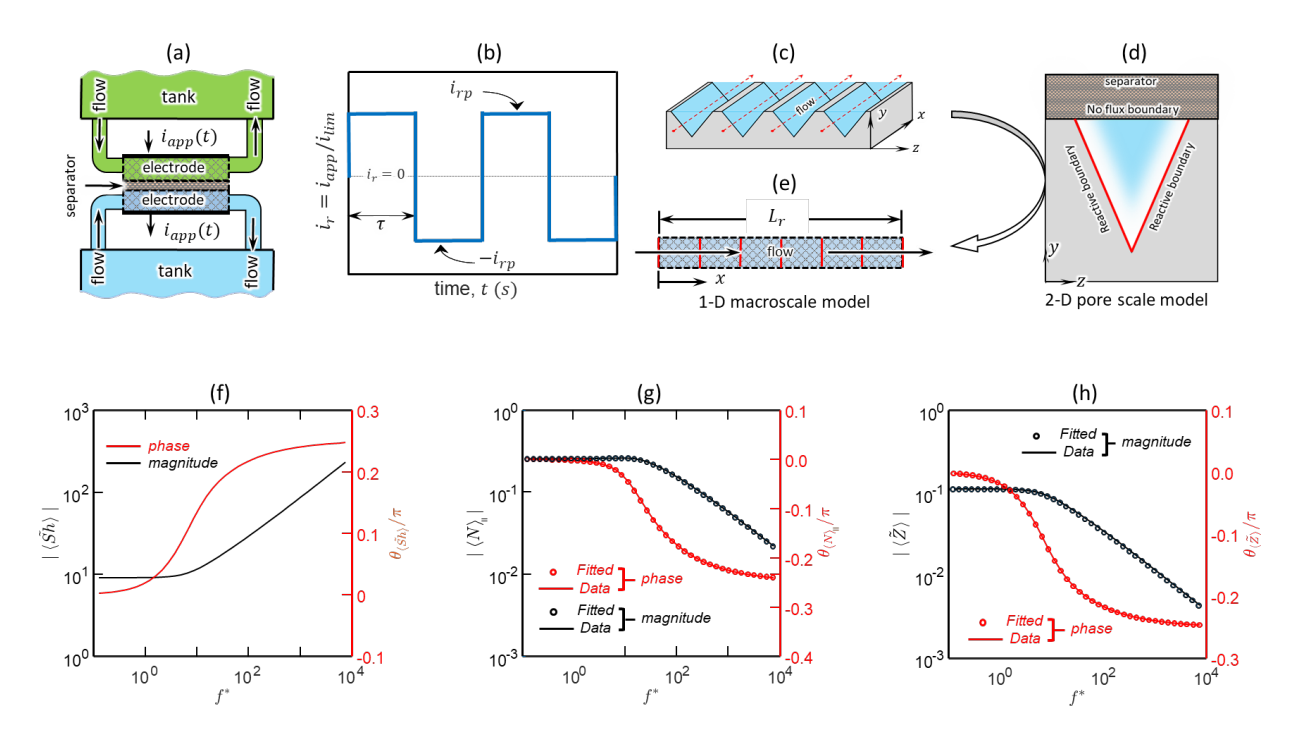


Fig. D2: (a) Experimental setup of flow cell, showing electrolyte flow circuits and electrode/separator/electrode staking inside of the reactor. (b) Schematic of applied current density variation with time for two steps of galvanostatic charging/discharging. (c) Magnified 3D representation of triangular channel engraved electrodes (TCEEs) with flow along channel length. (d) 2D pore scale model of TCEEs with different boundary conditions, reactive boundaries ($\mathbb{C}|_{S}=1$) and no flux boundary $\left(\frac{\partial \mathbb{C}}{\partial n}|_{S}=0\right)$. (e) 1D macroscale model of the electrode with electrolyte flow direction. Frequency dependence and fitting obtained from rational function approximation of different TFs calculated from numerical solution of pore-scale model, (f) spectral Sherwood number $\langle \widetilde{Sh} \rangle$, (g) parallel component of suppression vector $\langle N \rangle_{\parallel}$ and (h) $\langle \widetilde{Z} \rangle = 1/\langle \widetilde{Sh} \rangle$.

Table D1: Values of different parameters associated with flow cell experiments using triangular channel engraved electrodes (TCEE).

Parameter (unit)	Value/range
Volume-specific active area, $a (m^2/m^3)$	5.778×10^4
Limiting current density, i_{lim} (mA/cm^2)	10.1
Exchange current density, $i_0 (mA/cm^2)$	144.7
Mean residence time, t_r (sec)	0.82
Characteristic diffusion time, τ_d (sec)	11.6
Damköhler number, $Da(-)$	128.5
Péclet number, Pe (-)	7.05×10^{3}
Non-dimensional flow rate, β (–)	$2.4 \sim 0.3$
Tank-to-reactor volume ratio	2.56×10^{3}

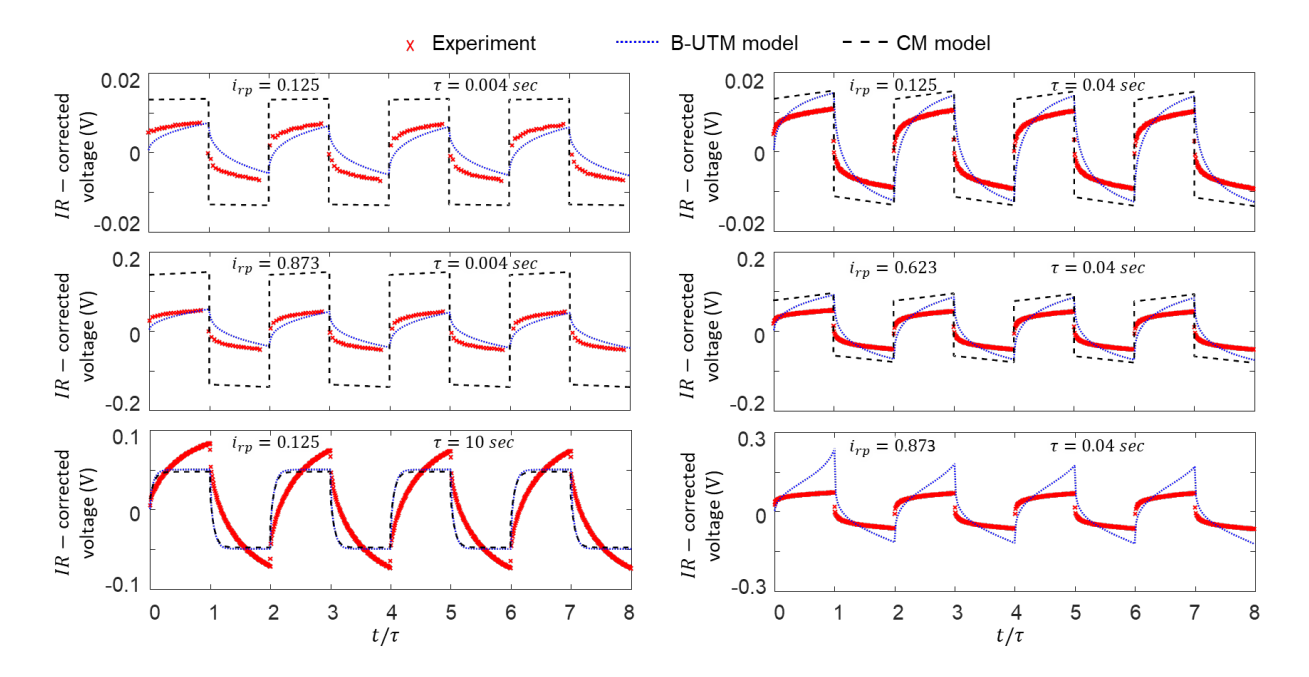


Fig. D3: Variation of *IR*-corrected cell voltage with time due to current applied with different i_{rp} and τ values.

For the model implementation, the local pore velocity (x-component u_x) field was obtained from numerical solution of the steady form of the x-component of the Navier-Stokes equations in the creeping flow limit:

$$\nabla \cdot (\nabla u_x^{\bullet}) = \frac{\nabla p}{\mu} \tag{D1}$$

with no-slip $(u_x^{\blacksquare}|_s=0)$ and impermeable $\left(\frac{\partial u_x^{\blacksquare}}{\partial n}\Big|_s=0\right)$ boundary condition at solid-solution interfaces, including the separator/solution interface. The local $\mathbb C$ field was obtained from

numerical solution of Eq. 4 from the main text by using a constant surface concentration condition at reactive interfaces ($\mathbb{C}|_s=1$), along with a no-flux condition $\left(\frac{\partial \mathbb{C}}{\partial n}\Big|_s=0\right)$ at the separator/solution interface (see Fig. D2d). From the numerical solution of these equations, the spectral Sherwood number $\langle \widetilde{Sh} \rangle$ and the parallel component of the suppression vector $\langle N \rangle_{\parallel}$ were calculated using Eq. 6 and Eq. 9. The variation of these TFs with non-dimensional frequency and their fitting from rational function approximation are shown in Fig. D2f-h. We note that, unlike arbitrary porous media, these TFs are independent of Pe because the velocity components along any direction perpendicular to channel length is zero (i.e., $u_y=u_z=0$). Finally, these TFs were embedded into the macroscopic model following an approach identical to that discussed in Sec. G to obtain the transient response of the flow cell (see Figs. D2c-e).

To study the transient response of this system, current was applied to the flow cell as a square wave with certain current magnitude and half-period τ (Fig. D2b). Figure D3 shows the time variation of IR-corrected voltage for different i_{rp} and τ values obtained from experiment and from predictions of the bottom-up transient model (B-UTM) along with conventional model (CM) predictions. A detailed discussion on Fig. D3 is in Sec. 3 of this article.

E. Discretization of pore-scale MCE, numerical implementation and verification

We model flow through a 2D microstructure's pores as a Newtonian, isochoric solution with constant dynamic viscosity and partial molar volume for each dissolved species. The molar-volume averaged velocity field u^{\bullet} is governed by creeping flow, assuming that the pore-scale Reynolds number Re = Pe/Sc is sufficiently small. These assumptions enable us to simulate u^{\bullet} using the time-independent, inertia-free version of the vorticity transport equation (VTE) $\nabla^4 \psi = 0$ [8], which is obtained by taking the curl of the Navier-Stokes equations. Here, ψ is a stream function from which the components of velocity automatically enforce conservation of volumetric flow rates ($\nabla \cdot u^{\bullet} = 0$): $u_{x}^{\bullet} = 0$ $\partial \psi/\partial y$ and $u_y^{\bullet} = -\partial \psi/\partial x$. The associated BCs at cylinder surfaces are enforced by the no-slip $(\partial \psi/\partial n|_s = 0)$ and impermeability $(\partial \psi/\partial s|_s = 0)$ conditions. We also require that no lift force is generated perpendicular to u_s , such that the Kutta-Joukowski [9] theorem requires fluid circulation Γ to vanish around each isolated solid in the domain: $\Gamma = \oint_{\mathcal{L}} u^{\bullet}$. $d{m s}=-\oint_c \;
abla^2\psi \; dA_{\scriptscriptstyle S} \; = 0. \;$ Periodic jump/fall BCs are also applied at unit-cell boundaries, $\psi(r+R) = \psi(r) + (R/|R|) \cdot \Delta \psi$. Here $\Delta \psi = \Delta \psi_x \hat{\imath} + \Delta \psi_y \hat{\jmath}$ is the periodic jump/fall in ψ across the unit-cell that results in a certain volumetric flow rate per unit depth equal to $|\Delta \psi|$. We used a second-order accurate finite difference method to discretize the VTE subject to the BCs already described, and we solved for ψ using a direct solver.

The equations that govern the transfer function $\mathbb{C}(\omega,r)$ (Eq. 4) were discretized using the finite volume method [10] using central differencing of advection and diffusion flux contributions at finite-volume cell faces subject to periodic BCs at unit-cell boundaries (i.e., $\mathbb{C}(r+R)=\mathbb{C}(r)$) and a unity Dirichlet condition at solid/solution interfaces. A complex-number, direct solver was used in MATLAB to obtain $\mathbb{C}(\omega,r)$ at the locations of

finite-volume cell centroids. The finite-volume cell dimensions Δx and Δy were selected to ensure that the corresponding grid-level Péclet numbers ($Pe_x = u_x^{\blacksquare} \Delta x/D$ and $Pe_y = u_y^{\blacksquare} \Delta y/D$) remained less than 0.5 to guarantee numerical stability subjected to the Courant–Friedrichs–Lewy condition [11].

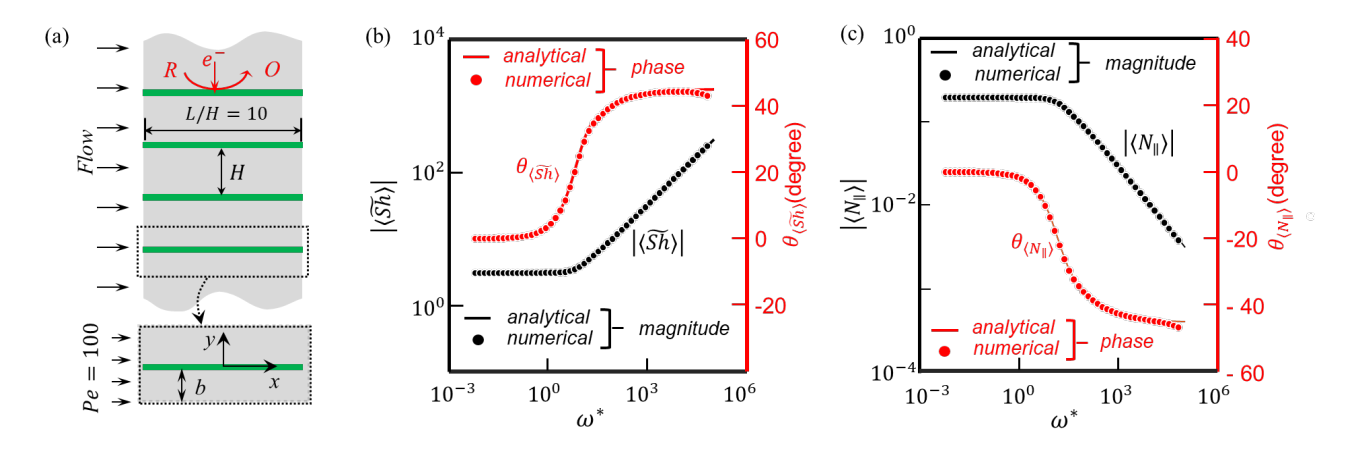


Fig. E1. (a) Domain of the parallel reactive boundaries used for verification of the present pore-scale numerical simulations. (b) and (c) respectively show the variation of analytical and numerical values for $\langle \widetilde{Sh} \rangle$ and $\langle N \rangle_{\parallel}$ with nondimensional angular frequency ω^* for the parallel reactive boundaries.

Here we present verification of our numerical scheme by comparing the obtained results with analytically derived results for a simple geometry, namely parallel reactive boundaries (PRBs). Fig. E1a shows a unit cell with a single boundary in the middle that repeats itself transversely to simulate an infinite array of pairs of parallel boundaries. The surface concentration is assumed to be uniform and to vary with time periodically following a sine function with angular frequency $\omega = 2\pi f$. For such a simple geometry analytical expressions for the volume-averaged concentration transfer function $\langle \mathbb{C} \rangle = \langle \bar{c} \rangle / \bar{c}_s$ and the spectral Sherwood number $\langle \widetilde{Sh} \rangle = b \langle \bar{l} \rangle_s / [D(\bar{c}_s - \langle \bar{c} \rangle)]$ were obtained as:

$$\langle \mathbb{C} \rangle = \frac{1}{\sqrt{j\omega^*}} \tanh(\sqrt{j\omega^*}) \tag{E1}$$

and,
$$\langle \widetilde{Sh} \rangle = \frac{\sqrt{j\omega^*} \tanh(\sqrt{j\omega^*})}{1 - \frac{1}{\sqrt{j\omega^*}} \tanh(\sqrt{j\omega^*})}$$
 (E2)

Here, frequency is nondimensionalized as $\omega^* = \omega b^2/D$, considering the gap between the boundaries as the characteristic dimension b. Further, the analytical expression for the streamwise component of transfer function $\langle N \rangle_{\parallel}$ was obtained as:

$$\langle N \rangle_{\parallel} = \frac{\left(\frac{3}{j\omega^*} + 1\right) \frac{1}{\sqrt{j\omega^*}} \tanh(\sqrt{j\omega^*}) - \frac{3}{j\omega^*}}{1 - \frac{1}{\sqrt{j\omega^*}} \tanh(\sqrt{j\omega^*})}$$
(E3)

The variations of both magnitude and phase in Figs. E1b and E1c for $\langle \widetilde{Sh} \rangle$ and $\langle N \rangle_{\parallel}$

respectively show excellent agreement between numerical simulation and the analytical solution, though at high frequency the numerical results deviate from analytical values because of the finite grid size used in numerical simulations. In practice we used a grid size of 1000×1000 cells in most cases to minimize computational expense. For high *Pe* cases more grid points were used to satisfy CFL criteria.

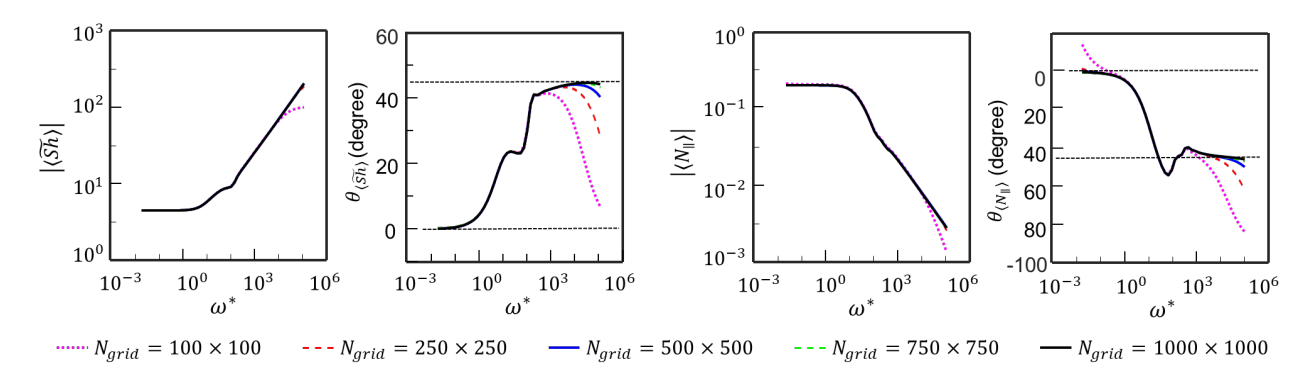


Fig. E2. Variation of $\langle \widetilde{Sh} \rangle$ and $\langle N \rangle_{\parallel}$ with ω^* that were obtained using different numbers of grid points applied to the periodic domain of cylinders depicted in Fig. 3c from the main text.

To check the grid dependence of our predictions for $\langle\widetilde{Sh}\rangle$ and $\langle N\rangle_{\parallel}$ simulations were performed for cylinder arrays at Pe=100 using different grids, the results of which are shown in Fig. E2. The most significant deviations among different grids were observed in the limits of low and high frequency. However, a grid of 1000×1000 cells adequately captures the fine-grid resolution while limiting computational expense.

F. Pore-scale concentration profiles

Here we analyze the shape of the concentration profiles at the midplane of the cylinder within a periodic array and along the direction transverse to the streamwise direction. To determine how frequency influences such profiles beyond that limit, the magnitude and phase $(\theta_{\mathbb{C}} = \tan^{-1}(\mathrm{Im}[\mathbb{C}]/\mathrm{Re}[\mathbb{C}]))$ of $\mathbb{C}(\omega,r)$ are shown in Fig. F1 on the same surface, defined by the red-dashed line shown in Fig. 3c from the main text. All profiles exhibit $|\mathbb{C}| = 1$ and $\theta_{\mathbb{C}} = 0$ at the solid/solution interface, consistent with the surface condition imposed in Eq. 4 from the main text. All profiles show a monotonic decrease of $|\mathbb{C}|$ toward zero as distance from the interface increases, while $\theta_{\mathbb{C}}$ increases monotonically with distance from the interface for all profiles, except those simulated at $Pe \gg 1$ with either $f^* \ll 1$ or $f^* \gg 200$. At any given location of interest all profiles show increased phase lag with increasing frequency, except for those simulated with $f^* \gg 200$ at $Pe \gg 1$. For $f^* \gg 200$ and $Pe \gg 1$ the non-monotonic variation of $\theta_{\mathbb{C}}$ with increasing distance and frequency is caused by the high rate of solute advection under such conditions. For $f^* \ll 1$ the lagless tracking of surface concentration causes $\theta_{\mathbb{C}}$ to vanish uniformly.

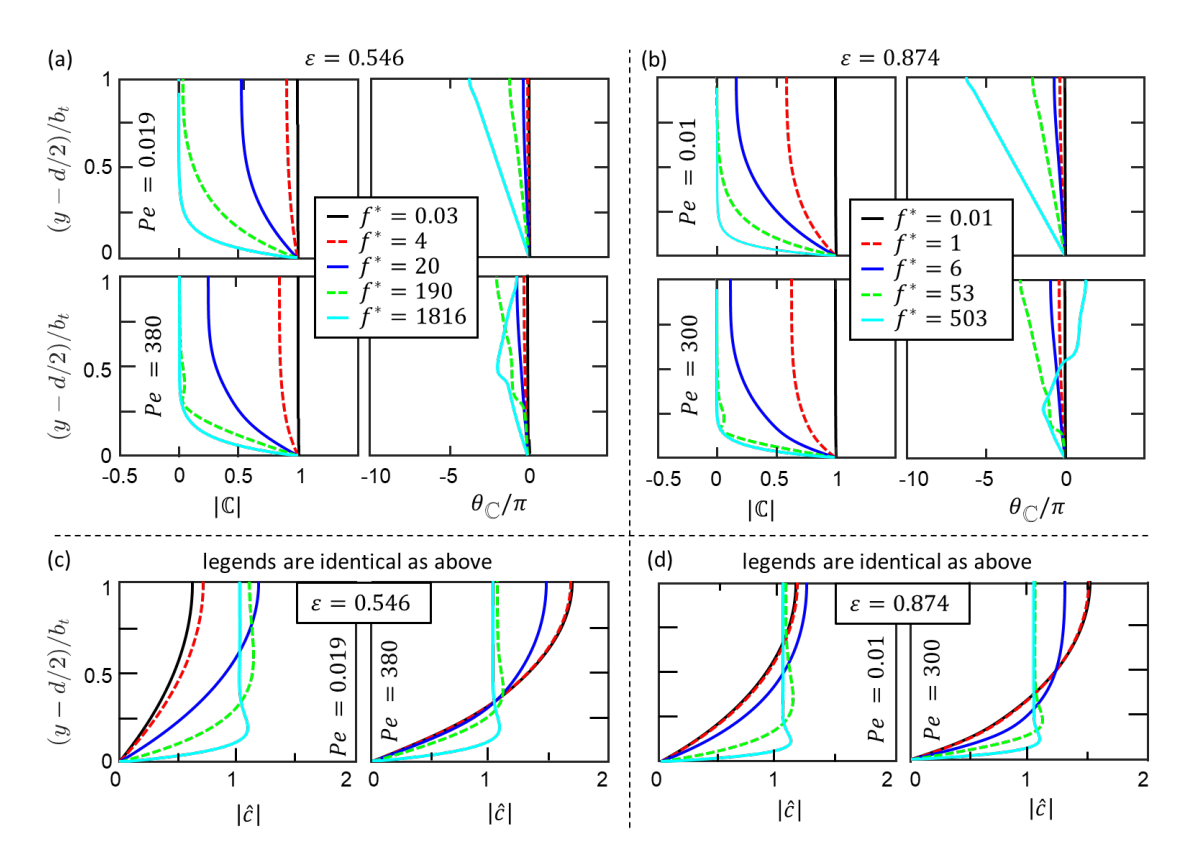


Fig. F1. Spatial variation of $|\mathbb{C}|$ and $\theta_{\mathbb{C}}$ in the transverse direction at the pore throat for (a) $\varepsilon=0.546$ with Pe=0.019 (first row) and Pe=380 (second row), (b) $\varepsilon=0.874$ with Pe=0.01 (first row) and Pe=300 (second). Spatial variation of $|\hat{c}|$ in the transverse direction at the pore throat for (c) $\varepsilon=0.546$ with Pe=0.019 (left) and Pe=380 (right), (d) $\varepsilon=0.874$ with Pe=0.01 (left) and Pe=300 (right).

The effect of Pe on system response in the low frequency limit $(f^* \ll 1)$ is not apparent from Figs. F1a and F1b as a result of the vanishing degree of spatial variation in \mathbb{C} that occurs in the limit of vanishing frequency. To compare the shape of concentration profiles in this limit at finite frequency we also calculated a non-dimensional concentration profile \hat{c} whose surface value is identically zero and whose volumeaveraged value is unity in the frequency domain: $\hat{c}(\omega, \mathbf{r}) \equiv (\bar{c} - \bar{c}_s)/(\langle \bar{c} \rangle - \bar{c}_s)$, which simplifies to $\hat{c}(\omega, \mathbf{r}) = (\mathbb{C} - 1)/(\langle \mathbb{C} \rangle - 1)$. Consistent with our findings deduced from Figs. F1a and F1b, the \hat{c} profiles in Fig. F1c and F1d reveal that the spatial extent of solution over which concentration varies decreases with increasing frequency, producing interfacial concentration gradients with magnitude that increases as frequency increases. Such a profile is reminiscent of the diffusion boundary layers that are observed in unbounded flows for sufficiently large frequencies. In addition, a negligible effect of Pe on these profiles is observed at sufficiently high frequencies ($f^* \gg 200$). In contrast, Péclet number influences profile shape substantially at sufficiently low frequencies ($f^* \ll$ 1), resembling the profiles obtained from simulations that we performed in the pseudosteady limit [1]. In summary, these results suggest that response in the low-frequency limit is controlled primarily by the dominant transport mechanism in the solution's bulk (pseudo-steady diffusion and/or advection), while response in the high-frequency limit is

controlled by transient diffusion through boundary layers of solution that exhibit frequency-specific thickness adjacent to interfaces.

G. Discretization of macro-scale MCEs and numerical implementation

We note that, while charging an RFB with known applied current variation $i_{ann}(t)$, the instantaneous local current distribution $i_{local}(\mathbf{r},t)$ inside the reactor is in general unknown. However, $i_{local}({m r},t)$ must satisfy the current-overpotential relation at the interface (Eq. 11 from the main text), and the mean of the distribution must be equal to the instantaneous applied current: $\langle i_{local}(\boldsymbol{r},t)\rangle=i_{app}(t)$. Since the solid phases are electronically connected to the current collector, the solution obtained from Eqs. 10 and 13 in the main text must reproduce the equipotential condition, which requires that the solid phase potential at every location inside the reactor is identical. We used this equipotential condition to develop an iterative algorithm where at each time step the initial distribution of local current was assumed to be uniform and equal to the instantaneous applied current distribution $i_{ann}(t)$. First, Eqs. 10 and 13 from the main text were discretized using the finite volume method to obtain a set of algebraic equations that are simultaneously solved to obtain $\langle c_i \rangle$ and $\langle c_i \rangle^T$ using a direct solver, where the face quantities were approximated using an up-wind scheme. Second, surface concentrations of both species were calculated from the local concentration polarization, which was obtained from the inverse Fourier transform of a rational transfer function approximation of the reciprocal of the spectral Sherwood number, defined as $\langle \tilde{Z} \rangle = 1/\langle \tilde{Sh} \rangle$, to obtain a state-space formulation in the time domain. Third, the local solid-phase potentials ϕ_s were calculated (Eq. 12) from local overpotential η values obtained by a Butler-Volmer (B-V) kinetics expression (Eq. 11). Lastly, the equipotential condition was checked within a specified nondimensional tolerance $(STD(\phi_S)/\langle \phi_S \rangle \leq 10^{-14})$. If not satisfied, the entire process was repeated for a subsequent iteration starting with the non-uniform, scaled local current distribution from last iteration. The scaling of current distribution was done to ensure that the obtained non-uniform current distribution had a mean value equal to the instantaneous applied current i.e., $\langle i_{local}(\mathbf{r},t)\rangle = i_{app}(t)$. This iterative process was repeated until the equipotential condition was satisfied. Then the algorithm proceeded to the next time step. The iterative algorithm is shown as a block diagram in Fig. G1.

Below are described each of the components of the numerical methods used for the macro-scale model.

• State space representation of transfer functions

Here we describe the step-by-step procedure to obtain the inverse Fourier transforms of the frequency dependent TFs to solve Eq.10 in the time domain. Since the associated PDEs and BCs are all linear, the system described here is a *linear time-invariant* (LTI) system [12,13]. Further, $\langle \widetilde{Sh} \rangle$ is a scalar quantity, and for uniform flow through symmetric (with respect to u_s) electrode microstructure, the transverse component of $\langle N \rangle$ is zero, i.e., $\langle N_{\perp} \rangle = 0$, which allowed us to define a single-input/single-output (SISO) state-space model (SSM) for both TFs separately. For such systems a rational transfer function $\langle TF \rangle$ can be expressed using its state space representation as:

$$\langle TF \rangle = C(j\omega I - A)^{-1}B + D \tag{G1}$$

Here, I is an identity matrix, and A, B, C, and D are the system matrices/vectors of the corresponding state-space model. The system matrices/vectors were obtained from the state-space representation that correlates the input u to the output y of the $\langle TF \rangle$ via a state vector x as governed by Eq. G2.

State equation:
$$\frac{dx}{dt} = A x + B u$$
 (G2a)

Output equation:
$$y = C x + D u$$
 (G2b)

The state matrix A consists of the poles p_i as non-zero elements along its diagonal. The input vector B is a column vector of ones. The output vector C is a row vector with residues r_i as its elements. D is zero for a proper transfer function, of which $\langle \widetilde{Z} \rangle$ and $\langle N \rangle$ are specific forms of. Since $\langle \widetilde{Sh} \rangle$ is improper $\langle \widetilde{Sh} \rangle (\omega \to \infty) \to \infty$ (Fig. 4) we define its reciprocal as $\langle \widetilde{Z} \rangle = 1/\langle \widetilde{Sh} \rangle$, which is a proper TF. We note that $\langle \widetilde{Z} \rangle$ represents the diffusional impedance of the system [14,15]. The input u and output y were taken from the definition of the corresponding TFs as shown in Table G1.

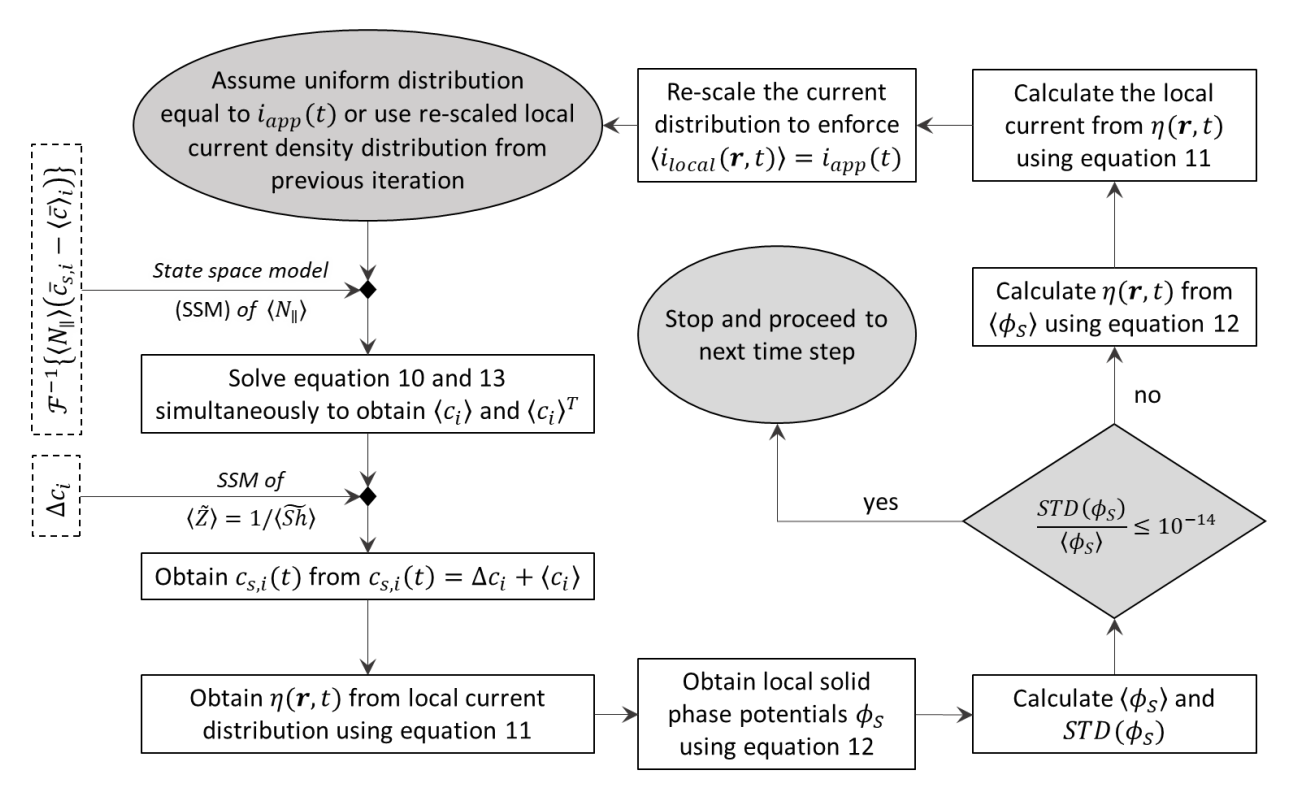


Fig. G1. Flow chart showing the steps in the self-consistent iteration algorithm used at each time step to solve macro-scale mass conservation equations (Eqs. 10 and 13 from the main text), while the equipotential condition is checked at each iteration using Eqs. 11 and 12 from the main text.

Table G1: List of input u and output y for various transfer functions to implement their corresponding state space model.

Transfer	Typo	Freque	Frequency domain		Time domain	
function	Type	Input u	Output y	Input u	Output y	
$\langle \tilde{Z} \rangle$	proper	$b\langle \bar{j}_i\rangle_s/D$	$\bar{c}_{s,i} - \langle \bar{c}_i \rangle$	$b\langle j_i\rangle_s/D$	$c_{s,i} - \langle c_i \rangle$	
$\langle N_{\parallel} \rangle$	proper	$\bar{c}_{s,i} - \langle \bar{c}_i \rangle$	$\varepsilon \langle \overline{W_i} \rangle / u_{\scriptscriptstyle S} $	$c_{s,i} - \langle c_i \rangle$	$\varepsilon \langle W_i \rangle / u_s $	

The poles p_i and the residues r_i of the TFs $\langle \tilde{Z} \rangle$ and $\langle N_\parallel \rangle$ were obtained from a rational function approximation with a finite number of poles (details in the following subsection). Equation F2 was discretized using an implicit scheme and solved at each time step for each finite volume cell by using a direct solver to obtain their corresponding state variables x and the outputs y in time domain, as shown in Table G1. First, the concentration polarization $c_{s,i} - \langle c_i \rangle$ was obtained from $\langle \tilde{Z} \rangle$ using instantaneous local current density (i.e., $b \langle j_i \rangle_s / D$) as input. Lastly, the covariance of velocity and concentration field $\varepsilon \langle W_i \rangle / |u_s|$ was obtained from $\langle N_\parallel \rangle$ considering $c_{s,i} - \langle c_i \rangle$ as input.

• Rational function approximation and vector fitting of transfer functions

To obtain the poles p_i and residues r_i , the TFs $\langle \tilde{Z} \rangle$ and $\langle N_{\parallel} \rangle$ were approximated as rational transfer functions with finite numbers of poles (Eq. G3).

$$\langle TF \rangle = \sum_{i=1}^{N} \frac{r_i}{i\omega - p_i} \tag{G3}$$

Here, N is the number of poles approximated, and $\langle TF \rangle = \langle \tilde{Z} \rangle$ or $\langle N_{\parallel} \rangle$. To obtain p_i and r_i a vector fitting algorithm [16-18] was used. This algorithm assumes an arbitrary initial guess for poles p_i , that makes Eq. G3 linear with r_i as unknowns. A set of linear algebraic equations for r_i was obtained by expressing Eq. G3 at each frequency sampled to yield an overdetermined linear system of equations Ax = b, where x is a column vector of unknown residues. This overdetermined problem was solved using a least-squares fitting technique. To improve the accuracy of the fitting these steps were repeated using an iterative scheme, where the initial guess of the poles in the subsequent iteration was updated by a new set of poles obtained from Eq. G3 using the residues from the previous iteration. Weighting functions were used for the least-squares fitting, based on the magnitude of data sampled at each frequency, so as TF values with small magnitude were given greater weight. Stable poles were ensured by changing the sign of the real part of the poles whenever necessary (i.e., pole shifting). To check the accuracy of the vector fitting algorithm, we reproduced the TFs using poles and zeros obtained from the vector fitting algorithm and compared with the original TFs values in Fig. G2. Vector fitting with N=30 poles/zeros resulted in excellent accuracy, where the reproduced TFs showed maximum deviation among all sampled frequencies less than $10^{-2}\%$ for all cases.

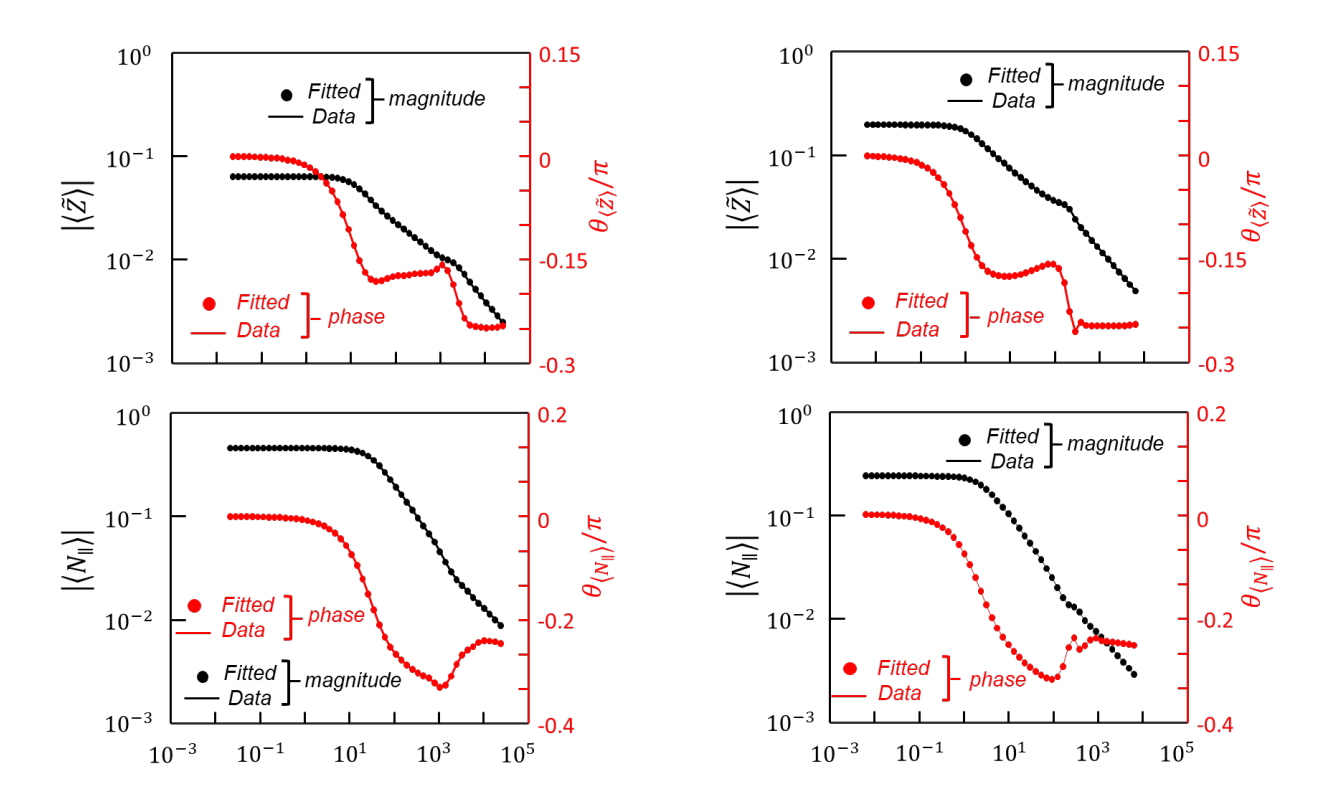


Fig. G2. Bode plot of the transfer functions $\langle \tilde{Z} \rangle = 1/\langle \tilde{Sh} \rangle$ and $\langle N_{\parallel} \rangle$ for $\varepsilon = 0.546$ (left panel) and $\varepsilon = 0.874$ (right panel) porosity electrodes. Pore-scale simulation data are shown as solid lines and the fitted data are shown in circles.

• Selection of time step size and number of finite volumes and verification of numerical implementation of the macroscopic model

Here, we present the dependence of the results on the time step size Δt and the number of finite volumes N_{FV} used in the one-dimensional macroscale model. Further, we used our TF embedded model to investigate the response for a finite diffusional space between two reactive parallel boundaries, for which analytical results were obtained by solving the associated MCEs in the time domain. The transient response of such a simple geometry obtained from the transient model introduced here is compared with the analytical results.

Selection of time step size and number of finite volumes

Figure G3a shows the variation of the numerically calculated volume-averaged concentration polarization with time step size Δt used in the numerical implementation. The absolute values of the volume-averaged concentration polarization are normalized by their arithmetic mean (as the figure is designated to show the variation in data only). The figure shows that for $\Delta t \leq 0.1 \, s$, the solution approaches an asymptotic value showing negligible dependence on Δt . In our calculations different values of Δt have been used $(10^{-6} \, s \leq \Delta t \leq 10^{-1} \, s)$ to minimize computation time, where smaller and larger Δt were used for short and large duration impulse simulations, respectively.

The finite volume discretization of associated MCEs ensures the conservation of mass for a finite-sized representative control volume. Thus, volume-averaged quantities did depend on the number of finite volumes N_{FV} used in the calculation. Thus, we show the dependency of the maximum polarization produced inside the reactor with N_{FV} in Fig. F3b. The data are normalized by their arithmetic mean to emphasize their variations. The results shows a negligible dependence of maximum polarization on N_{FV} for $N_{FV} \geq 50$ ($N_{FV} = 50$ produces deviation that is less than $10^{-1}\%$ compared to $N_{FV} = 200$). Consequently, we used $N_{FV} = 50$ in all simulations to minimize the computation cost while capturing the local maximum values with acceptable accuracy.

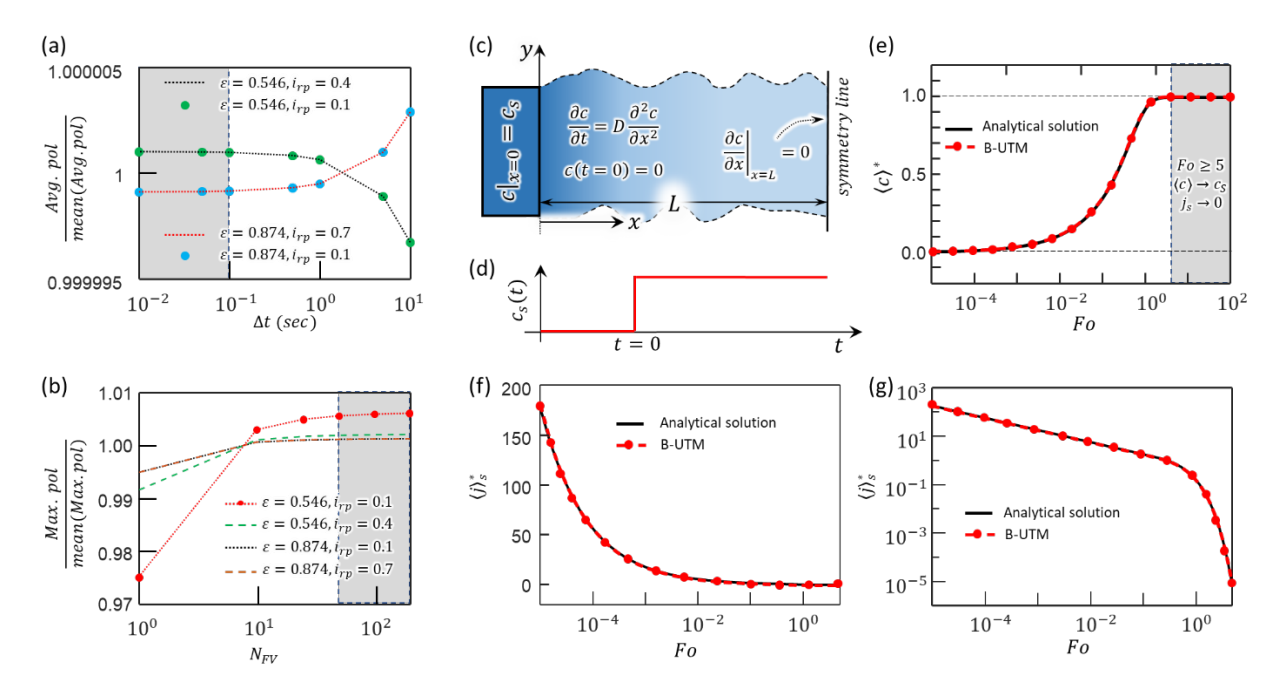


Fig. G3. (a) Time step dependence of numerical results for the macro-scale model. (b) Dependence of numerical results on number of finite volumes N_{FV} used in numerical simulations. (c) Schematic of the model used for model verification. (d) Variation of surface concentration c_s with time in the model shown in (c). (e) Comparison of volume averaged concentration $\langle c \rangle$ variation with Fourier number $Fo = Dt/L^2$ obtained from analytical solution and the bottom-up transient model (B-UTM). Comparison of time variation of the surface flux $\langle j \rangle_s$ obtained from analytical solution and B-UTM (f) in linear scale and (g) in logarithmic scale.

Verification of numerical implementation of the macroscopic model

In Fig. G3c we show the geometry of the simplistic problem used for model verification. Figure G3c shows a stationary finite diffusional space between two parallel reactive boundaries separated by distance 2L (length along y direction is considered infinite), where surface concentrations were varied identically by a step jump at time t=0, as shown in Fig. F3d [i.e., $c|_{x=0}=c|_{x=2L}=c_s(t)$]. Thus, the finite diffusional space enclosed can be considered as symmetric with respect to the midplane at x=L (i.e., $\partial c/\partial x|_{x=L}=0$). For such a problem the analytical solution can be obtained using

separation of variables. The analytical solution obtained is shown in Eq. F4 using nondimensional parameters.

$$c^* = 1 - \sum_{n=0}^{\infty} \frac{4}{(2n+1)\pi} \sin\left(\frac{(2n+1)\pi}{2}x^*\right) \exp\left(-\frac{(2n+1)^2\pi^2}{4}Fo\right)$$
 (G4)

Here, $c^*=c/c_s$, $x^*=x/L$ and the Fourier number $Fo=Dt/L^2$. The macroscopic response of the system can be observed from the time variation of non-dimensional volume-averaged concentration $\langle c^* \rangle = \frac{1}{L} \int_0^L c^* dx$ and the surface flux $\langle j \rangle_s^* = \frac{\langle j \rangle_s}{Dc_s/L} = -\partial c^*/\partial x^*|_{x^*=0}$ as shown by Eqs. G5 and G6.

$$\langle c \rangle^* = 1 - \sum_{n=0}^{\infty} \frac{8}{(2n+1)^2 \pi^2} exp\left(-\frac{(2n+1)^2 \pi^2}{4} Fo\right)$$
 (G5)

$$\langle j \rangle_{S}^{*} = 2 \sum_{n=0}^{\infty} exp \left(-\frac{(2n+1)^{2}\pi^{2}}{4} Fo \right)$$
 (G6)

For such a geometry, the analytical expressions for transfer functions $\langle \mathbb{C} \rangle$ and $\langle \widetilde{Sh} \rangle$ are shown in Eqs. E1 and E2, which were derived from the Fourier transform of the corresponding MCEs. Because $\langle \widetilde{Sh} \rangle$ is an improper transfer function, we defined its reciprocal as $\langle \tilde{Z} \rangle = 1/\langle \tilde{Sh} \rangle$ and obtained the macro-scale response of the system using the TF embedded transient model following identical approaches discussed earlier in this section (i.e., identical discretization, self-consistent iterative algorithm, state space representation, rational function approximation, and vector fitting). The results for $\langle c \rangle^*$ from the analytical solution and the B-UTM model are shown in Fig. G3e. The results show that the B-UTM matches the analytical solution for $10^{-5} \le Fo \le 10^{-2}$ with maximum deviation of 10^{-2} %. Meanwhile, for $Fo \ge 5$ the difference between the surface concentration c_s and volume-averaged concentration $\langle c \rangle$ becomes negligible with an infinitesimal flux at the interface. Thus, the variation of $\langle j \rangle_s^*$ obtained from the analytical solution and the B-UTM model are shown for $10^{-5} \le Fo \le 5$ on a linear scale (Fig. G3f) and on a logarithmic scale (Fig. G3g) to compare them in the low and high Fo limits. These curves show excellent agreement with maximum deviation of $2 \times 10^{-2}\%$ from the analytical results.

H. Multiple long duration impulses

When acceleration/suppression of reactive solute is accounted for as with our present bottom-up transient model (B-UTM), an initial step in current from open-circuit conditions causes the electrode to contain less reactant and more product in the bulk solution (Fig. 6 from the main text). Since the initial step lasts for the entire charging/discharging duration studied, the corresponding acceleration/suppression effect is not recovered. Rather, this pre-existing effect gets superimposed with the acceleration/suppression effect introduced later at $t/\tau=0$. A schematic of such superposition is depicted in Fig. H1 for a double-step transient in the applied current. For this illustration we assumed that the corresponding impulse time for both the impulses was large enough to approach the pseudo-steady limit (PSL).

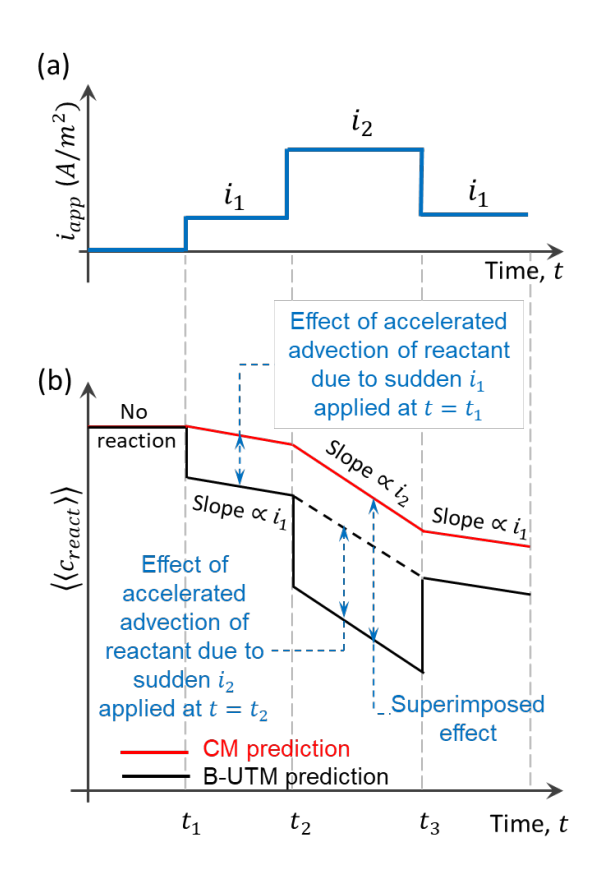


Fig. H1. Superposition of solute acceleration/suppression effect for multiple-step variation of input current.

Figure H1 shows the prediction from both the conventional model (CM) and the B-UTM model, where CM shows continuous change in reactant concentration with time. Meanwhile, B-UTM shows an abrupt change in $\langle\langle c_{reac}\rangle\rangle$ at the beginning of both the current steps, and during $i_{app}=i_2$ the observed effect has contributions from both transients. When current is returned to i_1 the acceleration/suppression, the partial contribution of the second transient vanishes immediately, while the partial contribution of the initial transient persists.

Supplementary References

- [1] M.A. Hamid, K.C. Smith, Modeling the Transient Effects of Pore-Scale Convection and Redox Reactions in the Pseudo-Steady Limit, J. Electrochem. Soc. 167 (2020) 013521. https://doi.org/10.1149/2.0212001jes.
- [2] H. Sarac, M.A. Patrick, A.A. Wragg, Physical properties of the ternary electrolyte potassium ferri-ferrocyanide in aqueous sodium hydroxide solution in the range 10-90°C, J. Appl. Electrochem. 23 (1993) 51–55.
- [3] J.C. Bazán, A.J. Arvia, The diffusion of ferro- and ferricyanide ions in aqueous solutions of sodium hydroxide, Electrochim. Acta. 10 (1965) 1025–1032. https://doi.org/10.1016/0013-4686(65)80014-7.

- [4] N.G. Tsierkezos, A. Knauer, U. Ritter, Thermodynamic investigation of ferrocyanide/ferricyanide redox system on nitrogen-doped multi-walled carbon nanotubes decorated with gold nanoparticles, Thermochim. Acta. 576 (2014) 1–8. https://doi.org/10.1016/J.TCA.2013.11.020.
- [5] K. Gong, F. Xu, J.B. Grunewald, X. Ma, Y. Zhao, S. Gu, Y. Yan, All-Soluble All-Iron Aqueous Redox-Flow Battery, ACS Energy Lett. 1 (2016) 89–93. https://doi.org/10.1021/acsenergylett.6b00049.
- [6] P. Kulesza, T. Jedral, Z. Galus, The electrode kinetics of the Fe(CN)63-/Fe(CN)64- system on the platinum rotating electrode in the presence of different anions, J. Electroanal. Chem. Interfacial Electrochem. 109 (1980) 141–149.
- [7] N. Frenzel, J. Hartley, G. Frisch, Voltammetric and spectroscopic study of ferrocene and hexacyanoferrate and the suitability of their redox couples as internal standards in ionic liquids †, Phys. Chem. Chem. Phys. 19 (2017) 28841–28852. https://doi.org/10.1039/c7cp05483a.
- [8] Y. Jaluria, K. Torrance, Computational heat transfer, Hemisphere Publishing Corporation, 1986.
- [9] J. Anderson Jr, Fundamentals of Aerodynamics, 2001. https://doi.org/10.1036/0072373350.
- [10] S. Patankar, Numerical heat transfer and fluid flow, CRC Press, 1980.
- [11] L. R., Courant, K., O., Friedrichs, H., On the partial difference equations of mathematical physics, IBM J. Res. 11 (1967) 215–234.
- [12] X. Hu, S. Stanton, L. Cai, R.E. White, A linear time-invariant model for solid-phase diffusion in physics-based lithium ion cell models, J. Power Sources. 214 (2012) 40–50. https://doi.org/10.1016/j.jpowsour.2012.04.040.
- [13] X. Hu, S. Stanton, L. Cai, R.E. White, Model order reduction for solid-phase diffusion in physics-based lithium ion cell models, J. Power Sources. 218 (2012) 212–220. https://doi.org/10.1016/j.jpowsour.2012.07.007.
- [14] T. Jacobsen, K. West, Diffusion impedance in planar, cylindrical and spherical symmetry, Electrochim. Acta. 40 (1995) 255–262. https://doi.org/10.1016/0013-4686(94)E0192-3.
- [15] A. Caprani, C. Deslouis, S. Robin, B. Tribollet, Transient mass transfer at partially blocked electrodes: a way to characterize topography, J. Electroanal. Chem. 238 (1987) 67–91. https://doi.org/10.1016/0022-0728(87)85166-5.
- [16] B. Gustavsen, A. Semlyen, Rational approximation of frequency domain responses by vector fitting, IEEE Trans. Power Deliv. 14 (1999) 1052–1059. https://doi.org/10.1109/61.772353.
- [17] B. Gustavsen, Improving the pole relocating properties of vector fitting, IEEE Trans. Power Deliv. 21 (2006) 1587–1592. https://doi.org/10.1109/TPWRD.2005.860281.
- [18] D. Deschrijver, M. Mrozowski, T. Dhaene, D. De Zutter, Macromodeling of multiport systems using a fast implementation of the vector fitting method, IEEE Microw. Wirel. Components Lett. 18 (2008) 383–385. https://doi.org/10.1109/LMWC.2008.922585.